Magma differentiation and rare metal mineralization of the Qongjiagang area, Himalayan orogen: evidence from trace element and boron isotope compositions of tourmaline

Haiquan Li [a,b] , Youye Zheng [c,d,*], Kirsten Drüppel [b], Peng Kang [e], Sonam Dolgar [e], Zongyang Jiang [e]

[a] *Institute of Geological Survey, China University of Geosciences, Wuhan 430074, China*
[b] *Institute for Applied Geosciences, Department for Mineralogy and Petrology, Karlsruhe Institute of Technology, Karlsruhe D-76131, Germany*
[c] *State Key Laboratory of Geological Processes and Mineral Resources and School of Earth Resources, China University of Geosciences, Wuhan 430074, China*
[d] *State Key Laboratory of Geological Processes and Mineral Resources, and School of Earth Science and Resources, China University of Geosciences, Beijing 100083, China*
[e] *Tibet Julong Copper Co., Ltd, Lhasa 850000, China*

ARTICLE INFO

ABSTRACT

Strongly fractionated granitic-pegmatitic rocks of the Qongjiagang area, Himalayan orogen are associated with economically important rare metal (e.g., Li, Nb, Be, and Ta) mineralization. Tourmaline is a frequent mineral in both the granites and pegmatites, which makes it an ideal candidate for investigating magmatic to hydrothermal processes that led to the rare metal enrichment. However, a systematic investigation of the response patterns of tourmaline compositions to differentiation processes is still lacking. In this study, we present petrographic and characteristics of the granitic-pegmatitic rock suites, as well as the chemical and boron isotopic compositions of tourmaline. Tourmalines in all samples exhibit schorl characteristics. Those from part of the muscovite granites exhibit pronounced zoning with highest MgO contents and $\delta^{11}B$ ratios being recorded by their cores ($\delta^{11}B$: -10.0 ~ -7.74 ‰) whereas the rims trend to lower $\delta^{11}B$ (-11.8 ~ -10.5 ‰). The $\delta^{11}B$ ratios of the tourmaline rims are close to those of unzoned tourmalines of the other muscovite granite samples (-12.5 ~ -12.1 ‰). Tourmalines of tourmaline granite (-14.5 ~ -13.9 ‰) and barren pegmatite (-14.0 ~ -12.9 ‰) exhibit comparably low $\delta^{11}B$ ratios. The ones in beryl pegmatites are characterized by the lowest $\delta^{11}B$ ratios (-15.7 ~ -14.3 ‰) but at the same time high concentrations of B_2O_5 and enrichment in Pb, Nb, Ta, and the light rare earth elements. Notably, tourmalines of spodumene pegmatites show variable $\delta^{11}B$ ratios (-14.6 ~ -10.3 ‰) and at the same time high values of Al_2O_3, B_2O_5, Li, Be, Sn, Cr, La, Ce, Pb, and Zn, yet low SiO_2. The textural position, as well as element and B isotope composition of tourmaline suggest a magmatic origin of all tourmalines, and record the magma differentiation from early muscovite granite to the subsequently formed pegmatites, with tourmaline of the spodumene pegmatite being subsequently altered by hydrothermal fluids. The variable composition of the tourmalines records independent enrichment of different rare metals during differentiation. Following this, tourmaline is a useful tool to reconstruct rare metal enrichment and mineralization processes controlled by granite magma differentiation and during interaction with externally derived fluids at the magmatic–hydrothermal transition.

1. Introduction

Rare metals (such as Li, Be, Nb, Ta, Sn, and W) are considered important resources that are critical for modern economies. They can be significantly enriched in granites and pegmatites, such as the Cuona-dong Be-Sn deposit (Li et al., 2017), the Gabo Li deposit (Li et al., 2022), the Qongjiagang Li deposit (Qin et al., 2021), and the Zhaguopu Li-Nb-Ta deposit (Zheng et al., 2024a) of the Himalayan orogenic belt. Among

---

those, the Qongjiagang Li deposit is a pegmatite-related deposit, characterized by a large volume of Li resources (Qin et al., 2021), and high concentrations of Be, Nb, and Ta. It is superexcellent area to research Magma differentiation and rare metal mineralization due there are more complete granite-pegmatite at Qongjiagang than other areas in the Himalayan orogenic belt. Although previous studies provided limited geochronological data and spatial relationships of the ca. 25–22 Ma granites and pegmatites (Liu et al., 2020), the mechanism of rare metals enrichment in the different rock types is yet poorly understood, mainly due to the lack of thorough studies on the mineralogy, petrology, and emplacement conditions of the associated granites. Several studies indicate that most of the granites and associated ore-bearing pegmatites in the Himalayan orogen contain tourmaline (Wu et al., 2020, Cao et al., 2022). Thus, the tourmaline may trace the granite-related rare metal mineralization.

Tourmaline is compositionally and texturally sensitive to its growth environment with a slow intracrystalline diffusion rate of major and trace elements (van Hinsberg et al., 2011b, Bosi, 2018). Thus, it is characterized by a high compositional variability and typically preserves complex compositional zoning patterns (Henry et al., 2011, van Hinsberg et al., 2011a, van Hinsberg et al., 2011b) that can be used to trace the magma/fluid sources and their evolution (Hu et al., 2018, Xiong et al., 2022, Chen et al., 2023, Zheng et al., 2024b). Thus, tourmaline can be a useful tool to trace the granite-related rare metals mineralization processes in the Qongjiagang area (Li et al., 2017, Wang et al., 2017, Wu et al., 2020). Recently, abundant research data indicate that the changing chemical compositions of tourmaline might reflect chemical changes in the respective evolving magmatic systems (Yang et al., 2015a, Zhou et al., 2019, Cheng et al., 2020, Hu et al., 2022, Xie et al., 2023). Especially, the $\delta^{11}B$ values of tourmaline are decreasing with magma differentiation yet increasing by fluid-rock interaction during hydrothermal alteration (Zhao et al., 2021, Xie et al., 2023, Yin et al., 2023, Zhang et al., 2024, Lv et al., 2025). Nonetheless, a systematic investigation of the changes of the tourmalinés chemical and isotopic compositions during differentiation processes is still lacking in the Qongjiagang area.

In case of the pegmatites, it is difficult to decipher the original magma composition. Whole rock geochemical data is often not representative for the composition of pegmatites due to their extremely large grain sizes and changes in the magma composition during fluid release and fluid-rock interaction in the pegmatite stage. Tourmaline is a promising tool to record both the magmatic evolution and the subsequent hydrothermal processes. Since a range of partition coefficients is recorded for trace-element partitioning between tourmaline and silicate melt based on experimental data and model calculations (van Hinsberg et al., 2011b, Huan et al., 2023, Ji et al., 2023), the composition of tourmaline can directly record the compositional signature of its host melt in magma-controlled systems (van Hinsberg, 2011, Cheng et al., 2022).

In this study, we present petrological data for a series of contemporaneously emplaced granites and pegmatites from the Qongjiagang area, Himalayan orogen as well as in-situ analyses of the major and trace element and B isotope composition of their respective tourmalines. The compositional variations of the tourmalines are used to trace the source and evolution of the granitic magma and the enrichment of rare metals. The results do not only provide insights into changes of the B isotope composition of tourmaline during magma differentiation and later hydrothermal fluid alteration, but also shed new light on the relations of the granites with pegmatite-type rare metals mineralization.

2. Geological setting and samples

2.1. Regional geological setting

The Himalayan orogen is one of the largest and best-known collisional orogens (Hodges, 2000, Yin et al., 2006, Kohn, 2014, Searle and

Treloar, 2019, Weller et al., 2021). It formed from subduction of the Indian continental crust and subsequent collision with the Eurasian plate along the Indus-Tsangpo suture zone after disappearance of the Neo-Tethys (Yin et al., 2006). It comprises four main litho-tectonic units (Yin et al., 2006), which are the Tethyan Himalayan (TH), the Greater Himalayan (GH), the Lesser Himalayan (LH), and the Sub-Himalaya (SH), from north to south (Fig. 1). Those tectonic units are separated by the South Tibetan Detachment System (STDS), the Main Central Thrust (MCT), and the Main Boundary Thrust (MBT), respectively.

Multiple magmatic-tectonic events are recorded for the Himalayan orogen (Wu et al., 2014, Wu et al., 2020, He et al., 2021, Cao et al., 2022, Wang et al., 2022), that are related to the Neo-Tethyan slab break-off in the early Eocene (49–40 Ma), the Indian lithosphere low angle underthrust in the late Eocene–early Oligocene (39–29 Ma), the Indian lithosphere lateral slab rollback in the late Oligocene–middle Miocene (28–15 Ma), the Indian lithosphere slab vertically tearing in the late Miocene (14–7 Ma), and the Indian lithosphere flat underthrust in the late Miocene–Pliocene–Pleistocene (6–0.7 Ma). In the Himalayan orogen, the TH and GH are the most crucial units to record its geological evolution.

The **TH** consists of Proterozoic to Mesozoic marine sedimentary rocks (such as clastic sediments and carbonate rocks) and low-grade metamorphic rocks. The sedimentary rocks were deposited at the passive margin of the northern Indian plate (Aikman et al., 2008). The TH is subdivided into two units based on rock type and metamorphic evolution. The southern part mainly comprises Proterozoic-Cenozoic marine sedimentary rocks of the Indian plate margin which underwent low-grade metamorphism at 23–17 Ma (Law et al., 2006). The northern part of the TH consists of three different rock units, i.e. deep-water sediments, flysch, and an ophiolitic mélange associated with the closure of the Tethys Ocean. This sequence was intruded by abundant Cenozoic granite bodies (Wu et al., 2020) that display an E–W-trending arrangement along the northern Himalayan margin (Hou et al., 2012, He et al., 2021, Ma et al., 2022, Gao et al., 2023).

The **GH** is an enormous nappe that formed as a result of subduction of the Indian plate and its subsequent collision with the Eurasian plate (Capitanio et al., 2010). It comprises amphibolite- to granulite-facies metasedimentary and *meta*-igneous rocks with minor late Proterozoic to Paleozoic marine sedimentary rocks (Singh, 2020). It was intruded by numerous Cambrian-Ordovician and Oligocene-Miocene (leuco-)granites (Wu et al., 2014, Wu et al., 2020, He et al., 2021, Cao et al., 2022, Wang et al., 2022).

There are obvious differences between the Cenozoic granites of the two different litho-tectonic units. Granitoids of the TH are characterized by more variable emplacement ages and compositions than those of the GH. Oligocene–Miocene granites of both belts have a high economic potential due to the occurrence of pegmatite-related rare metals deposits and mineralized granites (Li et al., 2017, Qin et al., 2021, Li et al., 2022, Zheng et al., 2024a). The recently discovered, giant Qongjiagang lithium deposit, including the study area, is situated within the GH leucogranite belt (Fig. 1). It comprises peraluminous and highly fractionated leucogranites and pegmatites with emplacement ages of 25–24 Ma, based on LA-ICP-MS U-Pb dating of monazite and columbite–tantalite (Zhao et al., 2021, Liu et al., 2020). The granitic-pegmatitic suites, which formed by crustal melting and underwent strong magmatic fractionation, partly show strong enrichment of columbite-tantalite, cassiterite, and beryl. Li mineralization is mainly found in spodumene pegmatites, which belong to the peraluminous LCT (Li-Cs-Ta-rich) pegmatite family. The rare metal enrichment of the granites and pegmatites is mainly attributed to extreme magmatic differentiation of the granitic magma and subsequent fluid release at the magmatic-hydrothermal transition.

2.2. Qongjiagang area

In the Rongxia valley-Qongjiagang mountain area (in the following summarized as Qongjiagang area), the major geological units exposed
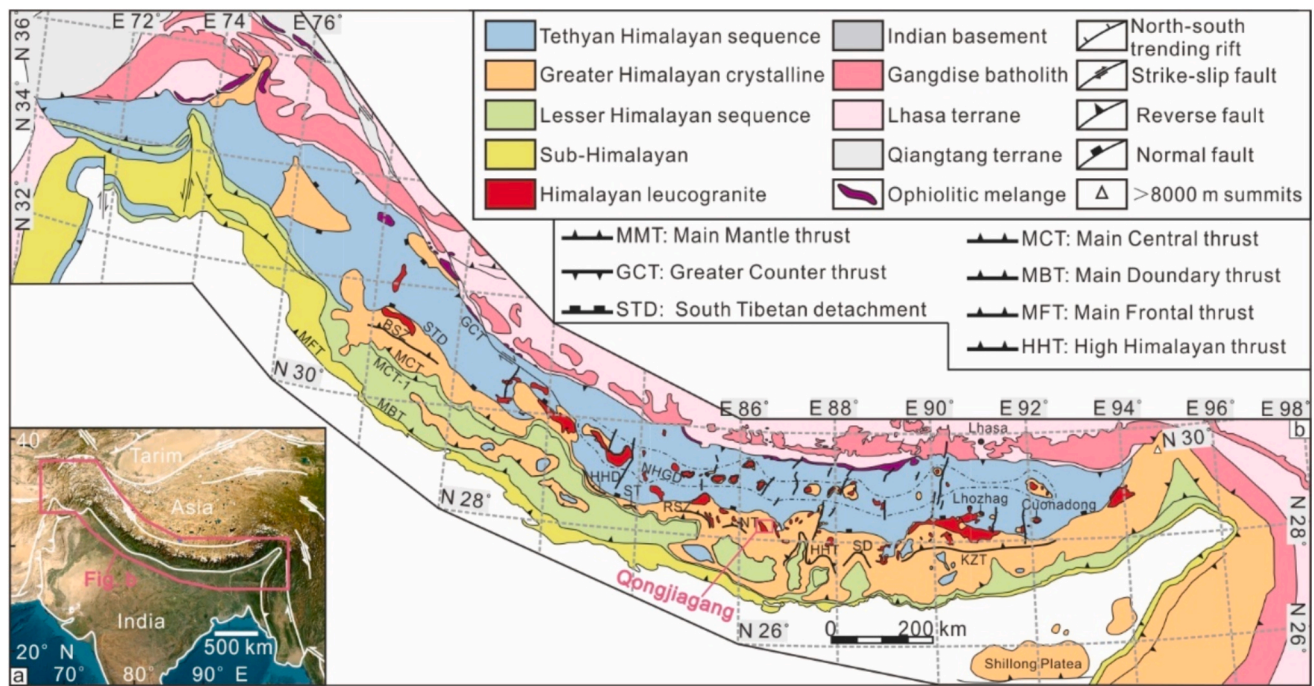
Fig. 1. (a) Topographic map of the Himalayan orogen and adjacent area, (b) Geological map of the Himalayan orogen (modified by Wang et al., 2022).

are the Jiangdong formation and the Rouqiecun group of the Greater Himalayan crystalline sequence (GH) (Figs. 2, 3). The Jiangdong formation is exposed in the southwestern part of this area. It mainly consists of a Proterozoic-Paleozoic metasedimentary suite and igneous rocks (Gou et al., 2017) which underwent Paleogene amphibolite to granulite facies metamorphism at ca. 47–29 Ma (Ding et al., 2019). The Rouqiecun group, a frequent Ediacaran-Cambrian unit in the Everest area, is exposed in the northeastern sector of the Qongjiagang area. The major rock types of this group are greyish-black biotite-bearing phyllite and calcareous quartzite, as well as younger quartz-rich marble intercalated

with minor phyllite. Cenozoic granites and associated pegmatites transect the metamorphic basement as dykes, veins, or small plutonic bodies which are emplaced along the Rongxia valley (NE-SW, Figs. 2, 3). Quaternary sediments cover most of the geological units.

The granites mainly comprise two-mica granite, muscovite granite, tourmaline granite, and albite granite. No clear contacts are observed between the different granite types (Fig. 2). **Two-mica granites** are distributed in the Rongxia valley and intruded the Jiangdong formation. Wall rocks mainly consist of marble, gneiss, and schist (Fig. 3a-c, e). **Muscovite granites** mainly occur in the Rongxia valley of the Cuore
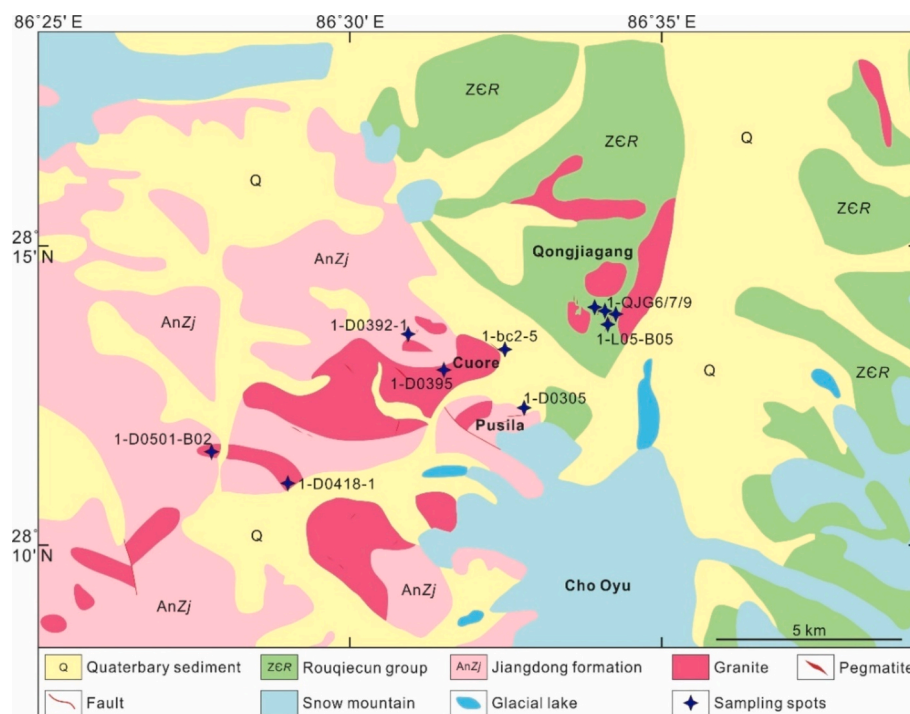

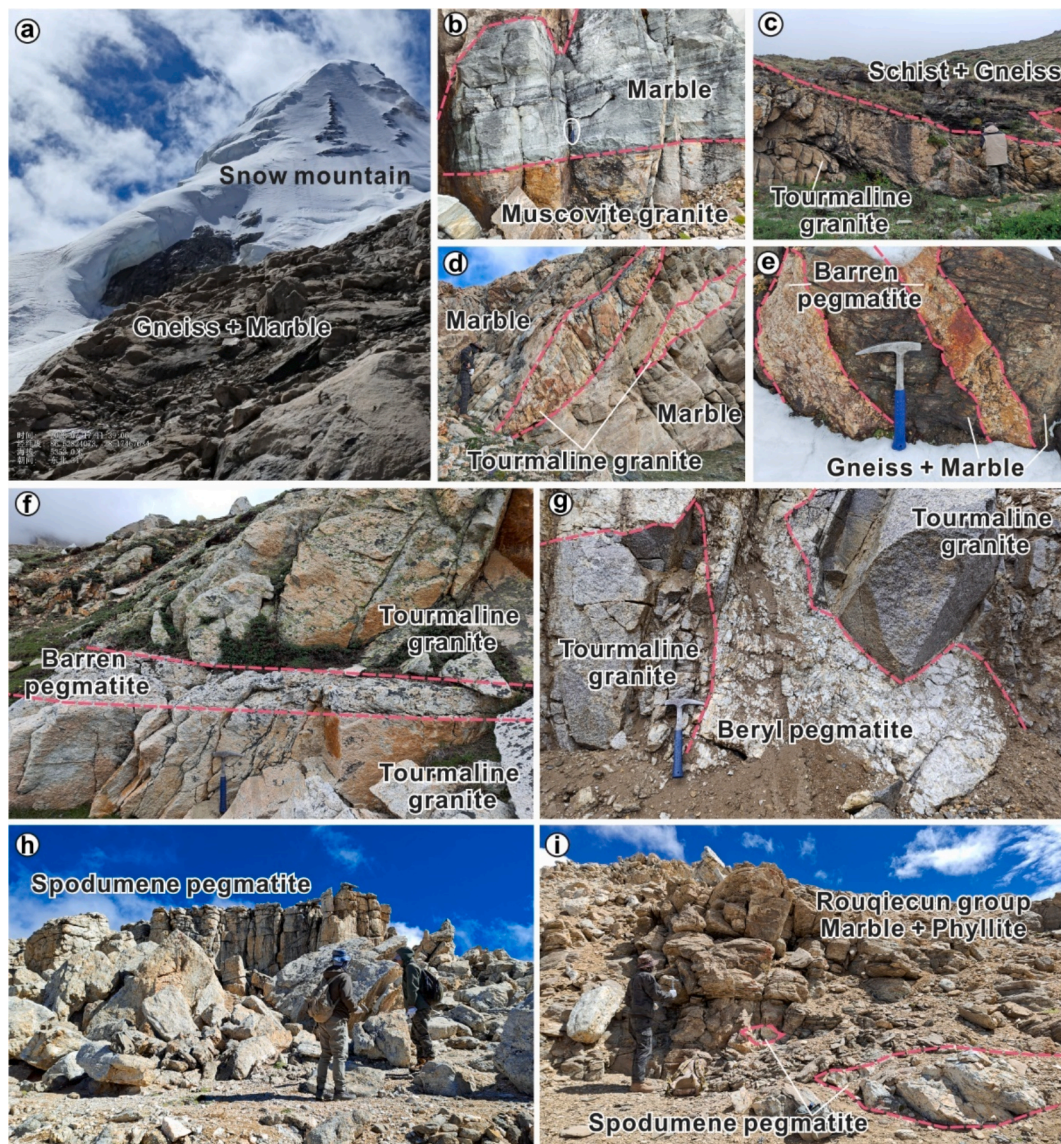Fig. 2. (a) The geological map of the Qongjiagang area.

Fig. 3. (a) The Jiangdong formation covered by snow at the western flank of Cho Oyu Mountain; (b) Plutonic bodies of muscovite granite intruded into marble of Jiangdong formation; (c-d) Veins and lenticular bodies of tourmaline granite transect gneiss and marble; (e-f) The barren pegmatite occurs within a granite body intruding the Jiangdong formation; (g) Beryl pegmatite veins transect the granite body; (h-i) Spodumene pegmatite veins and lenses intruded into marble and phyllite of the Rouqiecun group.

region, and also intruded the Jiangdong formation (Fig. 3b). The **tourmaline granites** intruded either the Jiangdong formation at Cuore or marble and phyllite of the Rouqiecun group at Qongjiagang (Fig. 3 d and i). The main wall rocks of the latter two granite types are gneiss and marble with some skarn developed at the granite-wall rock contacts (Fig. 3c-d). Among the pegmatites, **barren pegmatites** were discovered most frequently in Qongjiagang area, whereas **beryl pegmatites** were mainly found at Cuore and Qongjiagang. The barren and beryl pegmatites are in contact with both granite and metamorphic wall rock (Fig. 3e-g). The **spodumene pegmatites** are exposed at Cuore, Pusila, and Qongjiagang as veins or lenticular bodies emplaced within the Jiangdong formation and Rouqiecun group (Fig. 3h-i). They always occur in the vicinity of tourmaline granite.

3. Methods

3.1. BSE images and EDS major element data

The backscattered electron (BSE) images and major element

compositions of minerals were obtained using Tescan Vega SEM coupled with an Oxford EDS at the Karlsruhe Institute of technology (KIT). Analytical parameters are 20 kV voltage, and 1 μm spot size. Each mineral was measured at least three times.

3.2. Tourmaline LA-ICP-MS element analysis

Tourmaline major and trace element compositions were analyzed by LA-ICP-MS at the Wuhan SampleSolution Analytical Technology Co., Ltd., Wuhan, China. Detailed operating conditions for the laser ablation system and the ICP-MS instrument and data reduction are the same as those described by Zong et al. (2017). Laser sampling was performed using a GeolasPro laser ablation system that consists of a COMPexPro 102 ArF excimer laser (wavelength of 193 nm and maximum energy of 200 mJ) and a MicroLas optical system. An Agilent 7900 ICP-MS instrument was used to acquire ion-signal intensities. Helium was applied as a carrier gas. Argon was used as the make-up gas and mixed with the carrier gas via a T-connector before entering the ICP. A "wire" signal smoothing device is included in this laser ablation system (Hu et al.,

2015). The spot size and frequency of the laser were set to 42 μm and 5 Hz, respectively, in this study. Trace element compositions of minerals were calibrated against various reference materials (BHVO-2G, BCR-2G and BIR-1G) without using an internal standard (Liu et al., 2008). Each analysis incorporated a background acquisition of approximately 20–30 s followed by 50 s of data acquisition on the sample. The errors of all tested elements are lower than 2 %. An Excel-based software ICPMS-DataCal was used to perform off-line selection and integration of background and analyzed signals, time-drift correction and quantitative calibration for trace element analysis (Liu et al., 2008).

3.3. Tourmaline boron isotope analysis

Tourmaline B isotope compositions were measured by LA-MC-ICP-MS at the Wuhan Center of China Geological Survey, using the Neptune plus multi-collector coupled with a RESOlution S155-LR 193 nm laser ablation system. Analyses were carried out with a beam diameter of 43 μm, an energy density of 3.5 J/cm^2, and 5 Hz repetition rate. The analysis time is 90 s. The external standard is IMR-RB1 (Hou et al., 2010), the standard sample is NIST SRM 951, and the monitoring samples are 112566-Schorl and 98144-Elbaite,. In this study, all testing and calculation is based on sample-standard bracketing. Standard IMR-RB1 was used to emend the test results. The standard $\delta^{11}B$ ratios of IMR-RB1, 112566-Schorl, 98144-Elbaite is −12.22 ‰ ± 1.1 ‰ (P-TIMS), −12.50 ‰ ± 0.05 ‰, and −10.50 ‰ ± 0.20 ‰ (Dyar et al., 2001). All results from 112566-Schorl and 98144-Elbaite are in agreement with the standard data within the given error range.

3.4. EDX mapping of columbite-group minerals

The EDX mapping of columbite-group minerals was done by using electron probe microanalyzer in Wuhan SampleSolution Analytical Technology Co., Ltd., Wuhan, China. The instrument used is an JXA-8230 of JEOL with an accelaration voltage of 15 KV. The peak analysis time is 100 s, and the background analysis time 30 s. The calibration standard samples were provided by SPI company. We got Nb, Ta, Mn, and other major element images and displayed the mapping of Nb, Ta, and Mn element.

4. Results

4.1. Petrographic features and rare metal compositions

The petrographic investigation focused on the textural position of various rare metal-bearing minerals in the different granites and associated pegmatites of the Qongjiagang area. The **Muscovite granite** (Fig. 4a-d) is mainly composed of fine- to medium-grained quartz (~35 %), plagioclase (~30 %), k-feldspar (~20 %), muscovite (~10 %), and tourmaline (~4%). Accessory minerals comprise garnet, zircon, monazite, and apatite. The **tourmaline granite** (Fig. 4e-g) contains medium- to coarse-grained quartz (~35 %), plagioclase (30 %~35 %), k-feldspar (~20 %), tourmaline (~7%), and muscovite (total ~ 5 %). Accessory minerals include garnet, zircon, monazite, and apatite. The **barren pegmatite** (Fig. 4h-j) contains fine- to medium-grained quartz (~30 %), plagioclase (~25 %), k-feldspar (~30 %), muscovite (~6%), and biotite (~5%). Accessory minerals are tourmaline (~3%), garnet, zircon,
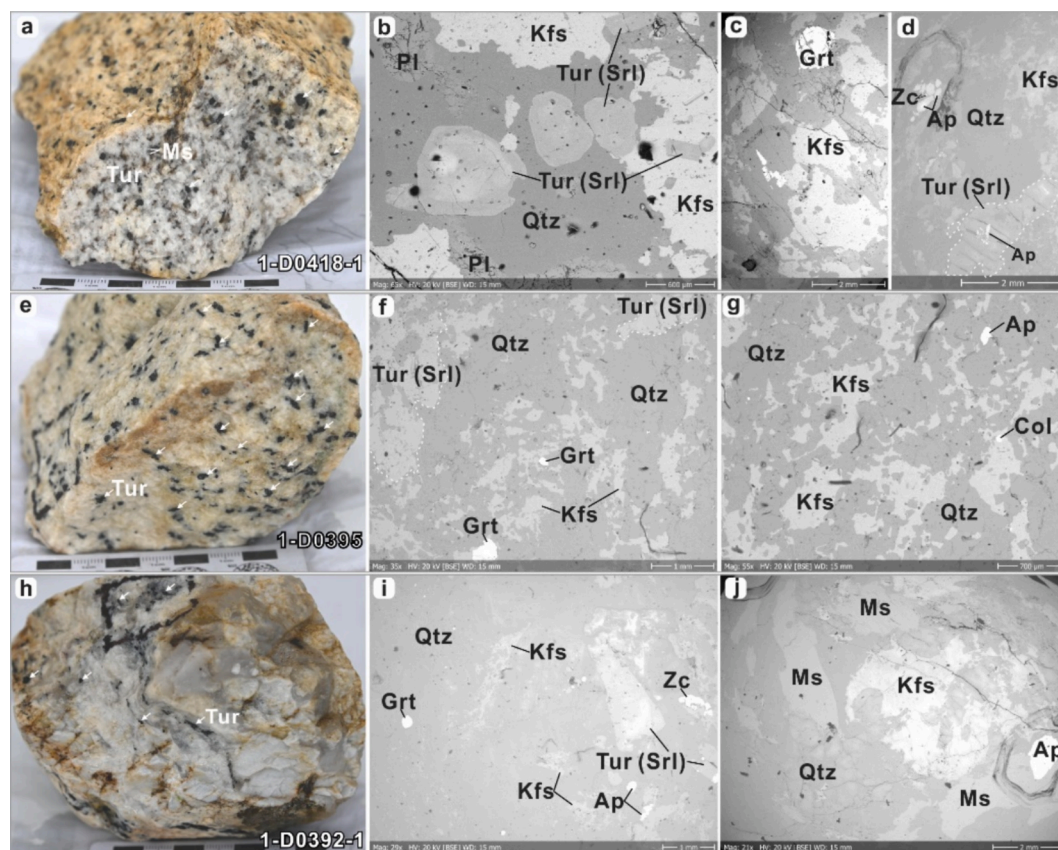

Fig. 4. Hand specimens and SEM-BSE images of muscovite granite (a-d), tourmaline granite (e-g), and barren pegmatite (h-j). (a) Tourmaline occurring together with magmatic minerals in muscovite granite hand specimens, (b) Tourmaline bordering quartz and k-feldspar, (c) Subhedral to anhedral garnet, quartz and k-feldspar, (d) Apatite inclusions in zircon and tourmaline. (e) Tourmaline is abundant in tourmaline granite, (f) Garnet inclusion in k-feldspar, (g) Columbite inclusion in k-feldspar associated with quartz and apatite, (h) Minor tourmaline occurring in barren pegmatite, (i) Accessory garnet, tourmaline, and zircon next to k-feldspar and quartz, (j) Apatite inclusion in muscovite, associated with k-feldspar and quartz. Abbreviations: Qtz—quartz; Pl—plagioclase; Kfs—k-feldspar; Ms—muscovite; Tur—tourmaline; Srl—schorl; Grt—garnet; Ap—apatite; Zc—zircon; Col—columbite.

monazite, apatite, and columbite-tantalite. The **beryl pegmatite** (Fig. 5a-g) comprises fine- to medium-grained quartz (~30 %), plagioclase (~20 %), k-feldspar (~30 %), beryl (~5%), and muscovite (~11 %). The accessory minerals comprise tourmaline (~3%), zinnwaldite, garnet, zircon, monazite, apatite, cassiterite, and columbite-tantalite. The **spodumene pegmatite** (Fig. 5h-p) is mainly composed of fine- to medium-grained quartz (~15 %), plagioclase (~20 %), k-feldspar (~35 %), and spodumene (20 %~30 %). Accessories are zinnwaldite (~3%), tourmaline (~2%), zircon, monazite, apatite, cassiterite, and columbite-tantalite. Notably, part of the muscovites record remarkably high Li contents (see below).

The Li_2O and $Nb_2O_5 + Ta_2O_5$ contents of barren pegmatite are 0.01–0.02 wt%, and 0.001–0.003 wt%, respectively. BeO contents are low. The Li_2O, BeO, and $Nb_2O_5 + Ta_2O_5$ contents are 0.07 wt%, 0.3 wt%, and 0.017–0.006 wt%, respectively, in beryl pegmatite, and 1.53–2.47 wt%, 0.03–0.08 wt%, and 0.004–0.025 wt%, respectively, in spodumene pegmatite (Table 1). Following this, the spodumene pegmatite is the major source for rare metals mineralization in the Qongjiagang area.

4.2. Tourmaline and accessory mineral textures

Rare metals-bearing accessory phases comprise tourmaline, garnet, columbite, cassiterite, zinnwaldite, beryl, and spodumene (Figs. 4-5). Tourmaline was mainly discovered in the granitic rocks. Hereby, the modal contents of tourmaline increase from muscovite granite to tourmaline granite. Remarkably, tourmaline exhibits a pronounced
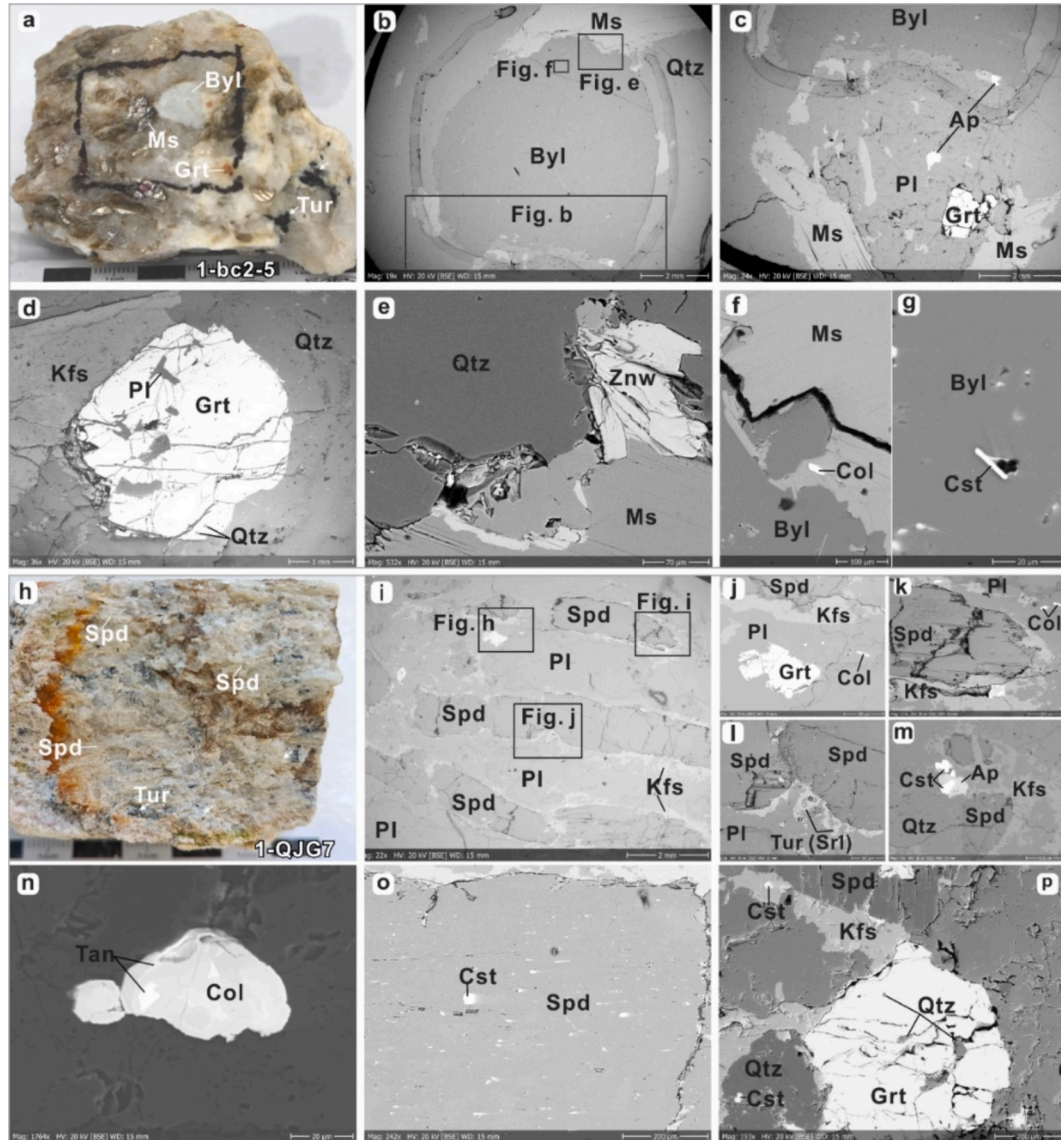

Fig. 5. Hand specimens and SEM-BSE images of beryl pegmatite (a-g) and spodumene pegmatite (h-p). (a) Tourmaline occurring together with other minerals in beryl pegmatite hand specimens, (b) Large beryl grain next to muscovite and quartz, (c) Garnet and apatite inclusions in plagioclase, associated with beryl and muscovite, (d) Garnet with plagioclase inclusions bordered by k-feldspar and quartz, (e) Zinnwaldite formation at the grain contact between muscovite and quartz, (f) Columbite inclusion in muscovite bordering beryl, (g) Inclusions of columbite and cassiterite in beryl, (h) Rare tourmaline occurring in spodumene pegmatite, (i) Intergrowth of plagioclase (with marginal k-feldspar) and spodumene, (j) Inclusion of anhedral garnet in plagioclase, (k) Spodumene bordering plagioclase (with a columbite inclusion); k-feldspar formation along the grain contacts, (l) Spodumene next to plagioclase. Grain contacts are marked by k-feldspar and tourmaline, (m) mineral aggregate of interstitial cassiterite and apatite, (n) columbite with marginal tantalite filling the intergranular space of quartz, (o) Large euhedral spodumene crystal with cassiterite inclusions, (p) Subhedral garnet with quartz inclusions next to quartz and feldspars; note the cassiterite inclusion in quartz. Qtz—quartz; Pl—plagioclase; Kfs—k-feldspar; Ms—muscovite; Znw—zinnwaldite; Tur—tourmaline; Srl—schorl; Grt—garnet; Ap—apatite; Zc—zircon; Byl—beryl; Spd—spodumene; Col—columbite; Tan—tantalite; Cst—cassiterite.

concentric zoning pattern with a core-rim texture visible in the BSE pictures of muscovite granite (sample 1-D0501-B02). In the pegmatites, the amount of tourmaline is generally low. The tourmaline crystals are euhedral to subhedral in the muscovite granites, tourmaline granite, barren pegmatite, and beryl pegmatite, whereas only subhedral to anhedral grains are observed in spodumene pegmatite (Figs. 4-6). Marginal dissolution of tourmaline is particularly observed in the spodumene pegmatite sample 1-L05-B05 (Fig. 6).

Rare garnet occurs as virtually unzoned euhedral crystals in all rock types and contains quartz and other mineral inclusions. Garnet itself is enclosed by magmatic phases like K-feldspar and quartz. The highest content and largest crystal size of garnet is recorded for the barren and beryl pegmatites (Figs. 4-5).

Columbite and cassiterite are uniformly distributed within individual samples and are mainly observed along the grain boundaries of the magmatic phases in muscovite granite, tourmaline granite, barren pegmatite, and beryl pegmatite. Moreover, they occur as inclusions in beryl and spodumene. Their modal content is remarkably high in the spodumene pegmatite, where they occur as mineral aggregates filling the intergranular space of spodumene crystals (Fig. 5h-i). Columbite is also observed as inclusions in the feldspars. Notably, some tantalite occurs as inclusions in the marginal zones of texturally early columbite in the spodumene pegmatite.

Zinnwaldite always occurs in the vicinity of muscovite in the beryl pegmatite, yet as independent crystals in the spodumene pegmatite. Beryl was observed in the tourmaline granite, beryl pegmatite (main occurrence), and spodumene pegmatite as remarkably large grains in direct grain contact with quartz and muscovite (Fig. 5). It contains
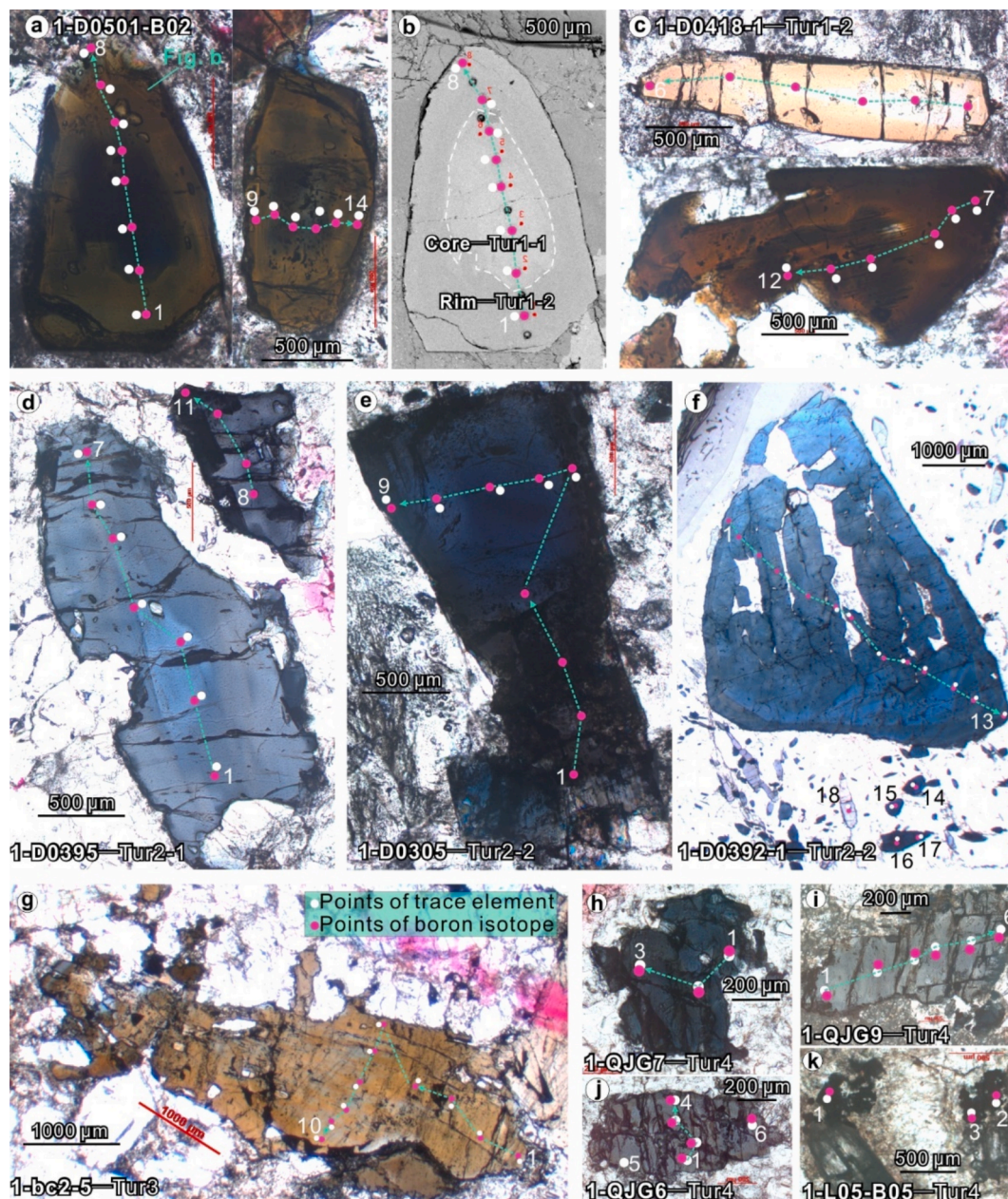

Fig. 6. Photo micrographs of tourmalines from different granites and pegmatites (a and c-k: PPL, b: SEM-BSE). The tourmalines were divided into four groups based on the respective rock types and tourmaline textures, i.e. Tur1 (Tur1-1 and Tur1-2) from muscovite granite, Tur2 from tourmaline granite (Tur2-1) and barren pegmatite (Tur2-2), Tur3 from beryl pegmatite, and Tur4 from spodumene pegmatite. The white and magenta points represent the locations of analyses of the major and trace element and boron isotope composition, respectively. The analysis number is marked in the figures, and stippled lines link the different spots of individual analytical sequences. (For interpretation of the references to colour in this figure legend, the reader is referred to the web version of this article.)

frequent inclusions of cassiterite. Abundant spodumene was only observed in the spodumene pegmatite (Fig. 5) where it forms large crystals intergrown with quartz, plagioclase, k-feldspar, tourmaline, garnet, apatite, cassiterite, and columbite-tantalite. It also contains inclusions of cassiterite.

4.3. Tourmaline major and trace element compositions

According to the classification of Henry and Dutrow (2011), most tourmalines belong to the alkali group and plot close to the (Na + K)-Ca-X-site vacancy connection line in the ternary diagram after (Hawthorne and Henry, 1999) (Fig. 7a), with rare samples crossing the border between the vacancy and alkali group fields. In the ternary 2Li-Fe-Mg diagram after Henry and Guidotti (1985) all tourmalines can be characterized as schorl with high Fe-contents (Fig. 7b, Henry and Guidotti, 1985). Moreover, they plot in the Na-rich schorl field in the Na/(Ca + Na)-Mg# diagram (Fig. 7c, Mg# = Mg/(Mg + Fe^{2+})), and in the Al-rich schorl field in the total Al-Mg# diagram after Henry et al. (2011) (Fig. 7d).

Notably, the tourmalines from different rock types show systematic differences in their compositions (Fig. 7, Table 2): (1) Tur1: The tourmalines display variable MgO (0.75–4.57 %) and FeO (9.37–14.3 %) contents. The major element compositions of tourmaline rims (Tur1-2) in the muscovite granite sample 1-D0501-B02 are close to those of unzoned tourmaline in the muscovite granite sample 1-D0418-1. Tourmaline cores (Tur1-1) are characterized by lower MgO, Al$_2$O$_3$, and CaO,

yet higher FeO contents (Fig. 8a-d). When compared to the other tourmaline types, Tur1 tourmalines are characterized by the highest average Mg# (molar Mg/(Mg + Fe)). (2) Tur2: The major element compositions of tourmalines from the tourmaline granite (Tur2-1, sample 1-D0395) and barren pegmatite (Tur2-2, samples 1-D0305 and 1-D0392-1) are characterized by higher Fe and lower Al contents than Tur1. (3) Tur3: Tourmaline of the beryl pegmatite (Tur3, sample 1-bc2-2) compositionally resembles Tur2. (4) Tur4: Tourmaline of the spodumene pegmatite (Tur4, sample 1-QJG6, 1-QJG7, 1-QJG9, and 1-L05-B05) is characterized by higher B$_2$O$_5$ (9.14–9.77 %, except an outliner), Li (0.24–0.58 apfu), total Al (6.22–6.89 apfu), and Na + K (0.72–1.98 apfu) contents, yet lower SiO$_2$ (35.2–39.7 %, except one outliner), and Na/(Ca + Na) ratios (0.75–0.93) when compared to tourmaline of other samples (Fig. 9a-c).

In Core zones (tur1-1) of Tur1 exhibit lower V, Co, and Ni, yet higher Zn contents than the rims (tur1-2; Fig. 8e-h). Tur3 is enriched in Be (5.85–13.1 ppm), Nb (0.69–1.87 ppm), Ta (0.13–0.73 ppm), and Sn (41.0–76.5 ppm) when compared to the other tourmaline types, and characterized by high Sr/Y ratios (283–642, except one outlier). Regarding their trace element concentrations, the Tur4 tourmalines of the spodumene pegmatite have the highest overall rare earth element (REE) contents (6.07–78.9 with a median of 15.9) and are characterized by a stronger fractionation of LREE over HREE than the other tourmaline types (Table 2). They are slightly enriched in Li (1736–4097 ppm), Be (4.39–16.3), Nb (1.02–3.61 ppm), Ta (0.48–2.52 ppm), Sn (49.2–102 ppm), Cr, La, Ce, Pb, and Zn contents (Fig. 9d-i), and show high Sr/Y
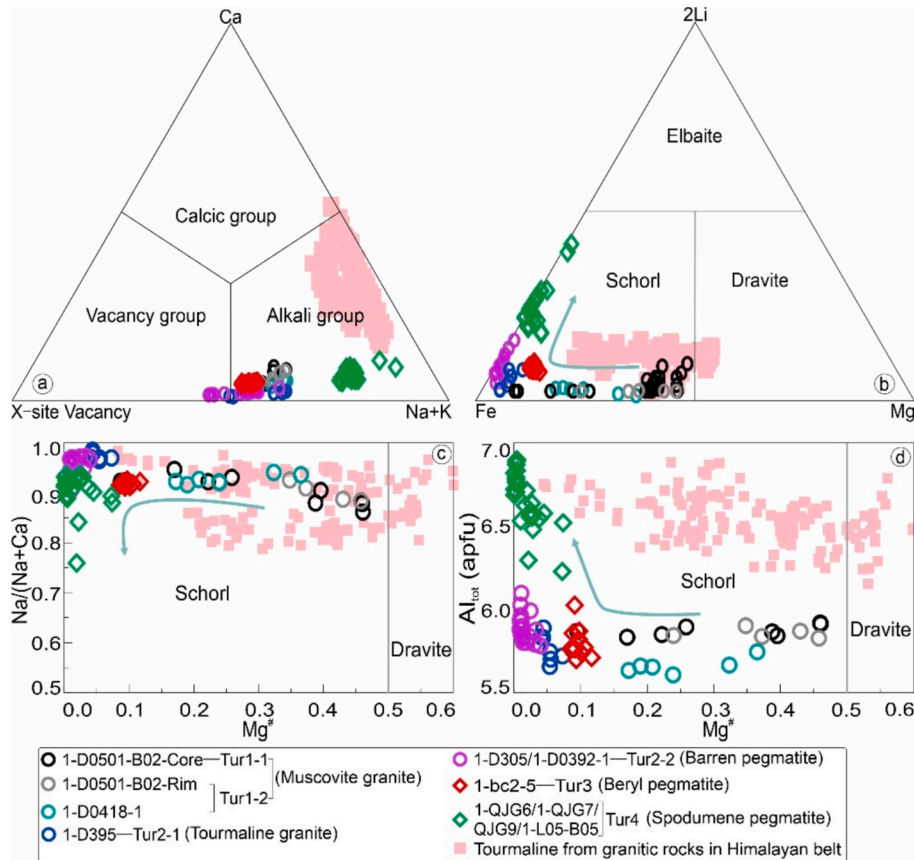

Fig. 7. Classification of the tourmalines from the Qongjiagang area. (a) Ternary Ca-X-site vacancy-Na + K diagram after Hawthorne and Henry (1999), (b) Ternary 2Li-Fe-Mg diagram after Henry and Guidotti (1985), (c) Na/(Na + Ca) vs. Mg# diagram after Henry et al. (2011), and (d) Al vs. Mg# diagram after Henry et al. (2011). Tur1-1 represents tourmaline cores in muscovite granite; Tur1-2 their rims as well as unzoned tourmaline from another muscovite granite sample; Tur2-1 is derived from tourmaline granite; and Tur2-2 occurs in barren pegmatite; and Tur3 in beryl pegmatite; Tur4 represent tourmalines from spodumene pegmatites. Green lines mark suggested trends of compositional changes of tourmaline from early muscovite granite to subsequently emplaced tourmaline, beryl, and spodumene pegmatite. Chemical data of tourmaline of granitic rocks from Cuonadong (Xie et al., 2023), Luozha (Cheng and Zhang, 2024), and Nyalam (Yang et al., 2015a) in the Himalayan belt are plotted for comparison.
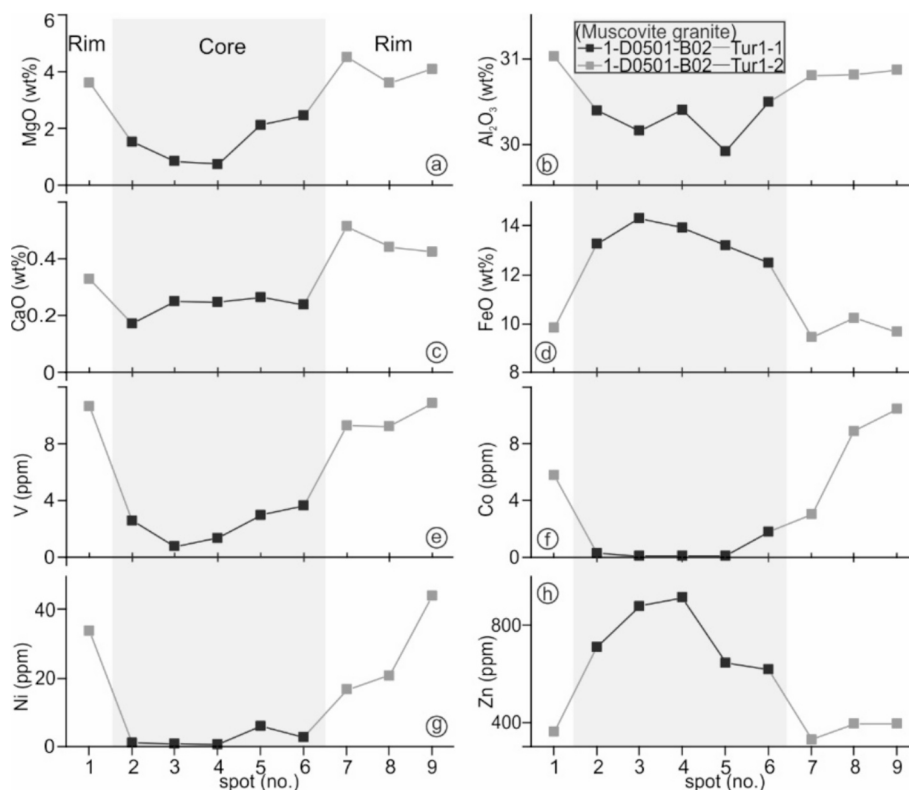
Fig. 8. Major (a-d) and trace element (e-h) zoning patterns of tourmalines in muscovite granite (sample 1-D0501-B02).

ratios (355–1573, except two outliers).

Notably, the (Na, Mg) $(X_{vacancy} + Al)_{-1}$ substitution mechanism is dominant for Tur1 to Tur3 (Fig. 10), yet Tur4 exhibits a different substitution scheme (Fig. 10a, c). A trend of increasing Fe, Na, K, and Li is observed for tourmalines of successively emplaced granitic rocks whereas the Mg content remains almost constant.

4.4. Boron isotope compositions of tourmaline

Variable but systematic changes in the B isotope ratios are recorded for tourmaline in the successively emplaced granites and pegmatites from the Qongjiagang area (Fig. 11, Table 3).

Cores of tourmaline in muscovite granite (Tur1-1) show the highest average $\delta^{11}B$ ($\delta^{11}B = {}^{11}B/{}^{10}B$) values ranging from −10.0 to −7.74 ‰, with a mean of −8.88 ‰. Rims of zoned tourmaline crystals and unzoned tourmaline of the muscovite granite (Tur1-2) show lower $\delta^{11}B$ values of −12.8 to −10.5 ‰, with a mean of −12.1 ‰. Tourmaline from tourmaline granite (Tur2-1) shows $\delta^{11}B$ values of −14.5 to −13.7 ‰, with a mean of −14.1 ‰. The $\delta^{11}B$ values of Tur2-2 from barren pegmatite range between −14.0 and −12.6 ‰, with a mean of −13.2 ‰. The $\delta^{11}B$ values of tourmaline from beryl pegmatite are comparably low, ranging from −15.7 to −14.3 ‰, with a mean of −15.2 ‰, whereas those of tourmaline from spodumene pegmatite (Tur4) are strongly variable (14.6 to −10.3 ‰).

All analyzed $\delta^{11}B$ values are within the range of those known from other rock types of the Himalayan orogen (Fig. 12). Hereby, Tur1 displays the highest isotopic ratios in the Qongjiagang granite-pegmatite system, which are close to values of tourmaline from Himalayan metapelite (−12 ‰ to −9‰, Figs. 11-12) provided by Ji et al. (2023). From Tur1 to Tur3, a gradually decrease of the $\delta^{11}B$ values can be observed, whereby Tur3 displays the lowest isotopic ratios of all tourmalines of the Qongjiagang granite-pegmatite system (Figs. 11-12). Remarkably, the $\delta^{11}B$ values of tourmaline from the late spodumene pegmatite (Tur4) deviate from this trend, exhibiting strongly variable $\delta^{11}B$ values, which are mostly even higher than those of Tur3 (Figs. 11-12).

4.5. Columbite-group minerals from spodumene pegmatite

Columbite-group minerals (CGMs) primarily occur in pegmatites. In particular, the compositions are abundant in spodumene pegmatite where the CGMs typically form euhedral-subhedral crystals that are commonly intergrown with quartz, mica, and spodumene. In addition, they occur as rare tiny inclusions in mica and plagioclase. BSE imaging and EDX mapping of these grains reveal three distinct types of crystals (Fig. 13). Type 1 with a Nb-rich core and Ta-W-rich rims (Fig. 13a-d), type 2 crystals with distinct chemical textures which ones (Fig. 13e-h). and finally type 3, which are characterized by no-zoning and cluttered chemical textures (type 3, Fig. 13i-m).

5. Discussion

5.1. Origin of tourmalines

The tourmalines investigated in this study were subdivided into four groups based on the tourmaline textures and their major and trace element compositions (Figs. 7-10). All tourmaline crystals are homogeneously distributed in their respective rock samples. They are subhedral in the muscovite granite, tourmaline granite, barren pegmatite, and beryl pegmatite (Tur1-3), yet subhedral to anhedral due to marginal dissolution in spodumene pegmatite (Tur4). The tourmalines textural occurrence suggests that the tourmaline is magmatic in origin but, in case of Tur4, was affected by hydrothermal alteration (Fig. 6).

The major element compositions of all analyzed tourmalines correspond to schorl with high Na + K and Al contents (Fig. 7). The tourmalines display high Li and Sn contents, Li/Sr ratios, yet low Cr and V contents (Fig. 14), consistent with the commonly observed characteristics of magmatic tourmaline (Zhao et al., 2019, Harlaux et al., 2020, Yu et al., 2024). Remarkably, the $\delta^{11}B$ values of Tur1 tourmaline cores are close to those of metapelites in the Himalayan area (Ji et al., 2023) (Figs. 11-12), suggesting that the granitic rocks hosting the tourmaline formed from partial melting of a metapelitic source. This interpretation
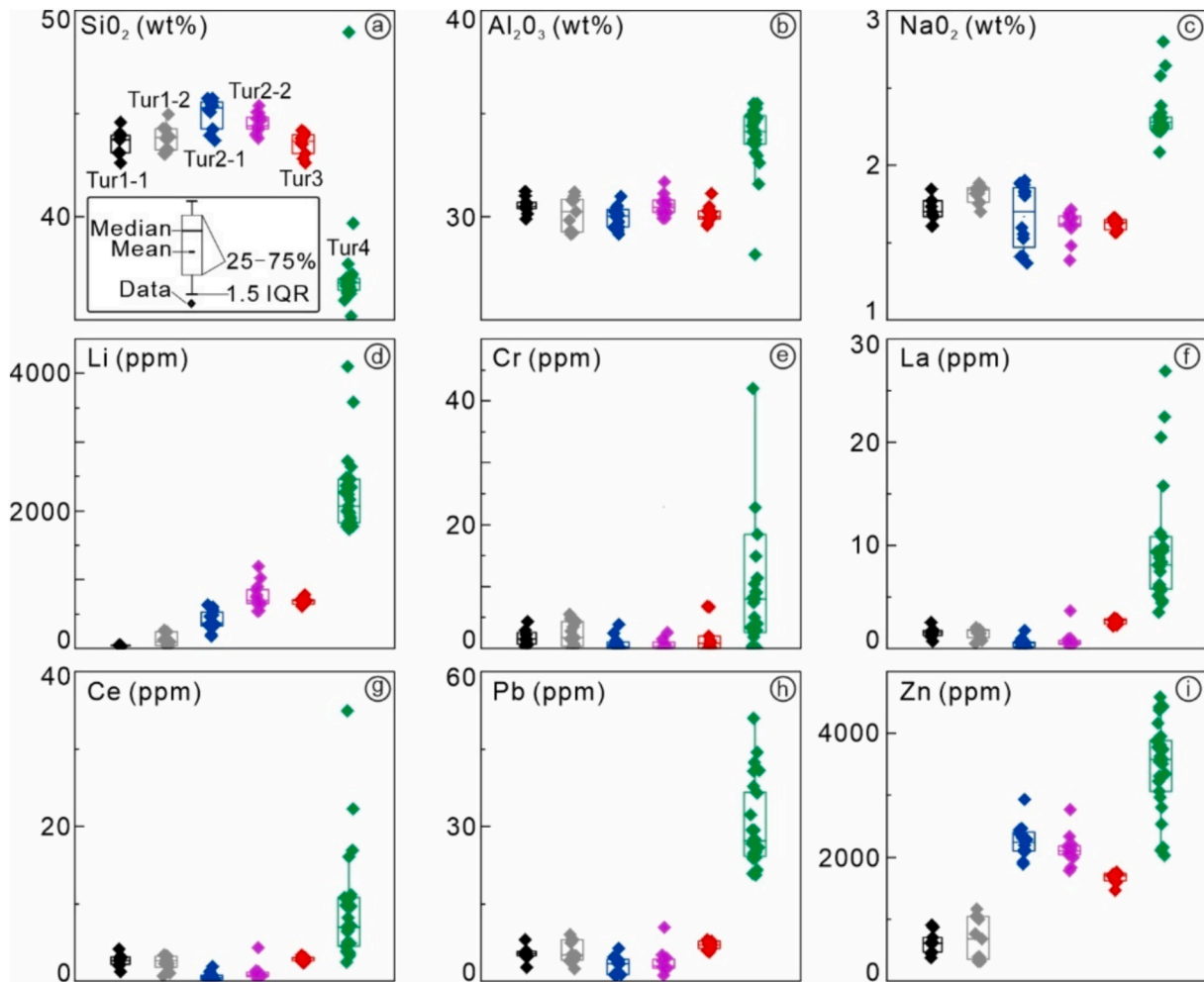
Fig. 9. Major and trace element compositions of the different tourmaline types from the granites and pegmatites of the Qongjiagang area. (a-c) Tur4 displays lower SiO$_2$, yet higher Al$_2$O$_3$ and Na$_2$O contents than other type tourmalines, (d-i) The Li, Cr, La, Ce, Pb, and Zn contents of Tur 4 are higher than those of the other type tourmalines.
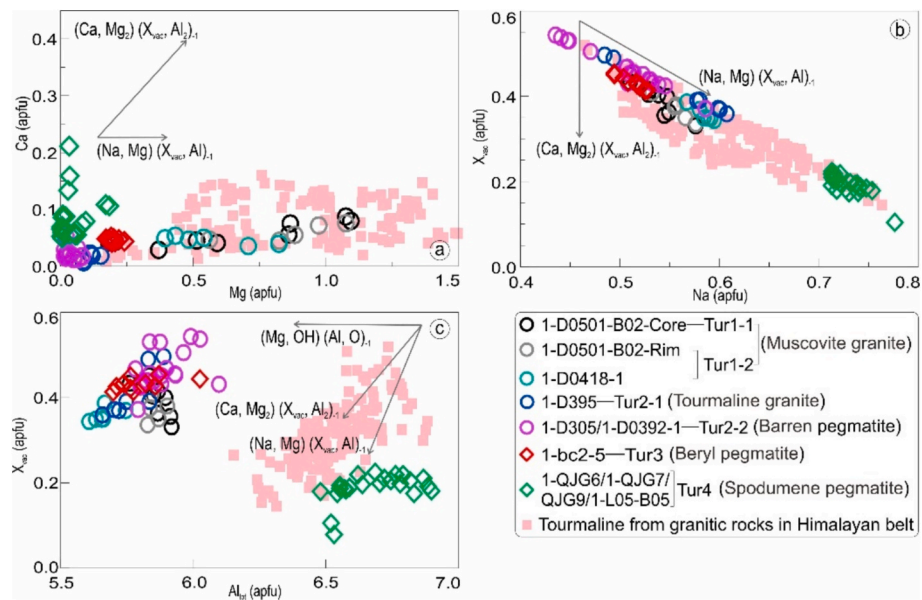

Fig. 10. Substitution schemes of tourmalines, illustrating the trends proposed by Liu et al. (2022). (a) X-vacancy vs. Na diagram, (b) X-vacancy vs. Al diagram, (c) Ca vs. Mg diagram.
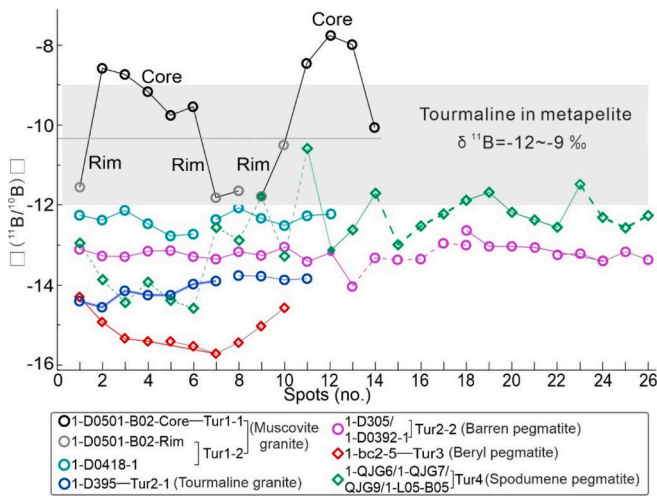
Fig. 11. The boron isotope values of the different tourmaline types from granites of the Qongjiagang area. The grey area represents the boron isotopic composition of tourmaline from metapelite of the Himalayan orogen.
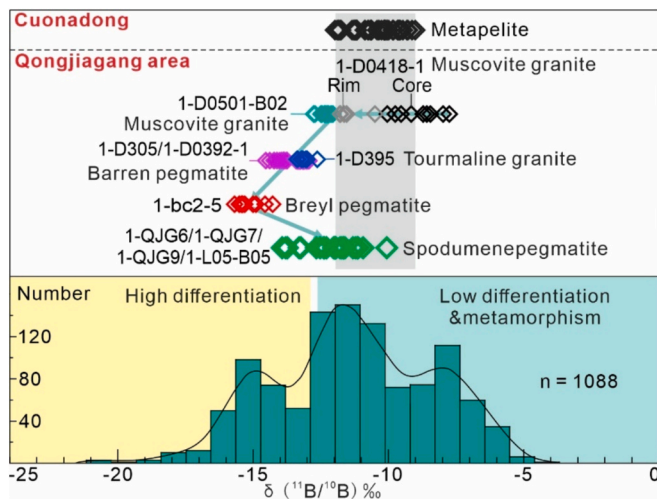

Fig. 12. The boron isotope values of the different tourmalines from granites and pegmatites of the Qongjiagang area compared to the overall boron isotope composition of metapelites (black diamonds) and of granitic rocks from the Greater-Tethyan Himalayan belt (histogram). The isotopic data of the granitic rocks defines normal distribution of boron isotope values with three peaks. Hereby, low boron isotope values on the right represent strongly differentiated granitic rocks, whereas high boron isotope ratios on the left mirror granites that underwent less differentiation. Boron isotope data of the histogram are mainly derived from tourmaline of High-Tethyan Himalayan granitic rocks (Chaussidon and Albarède, 1992, Yang et al., 2015a, Gou et al., 2017, Zhou et al., 2019, Cheng et al., 2020, Han et al., 2020, Fan et al., 2021, Hu et al., 2022, Liu et al., 2022, Fan et al., 2023, Ji et al., 2023, Xie et al., 2023, Cheng and Zhang, 2024).

is supported by the available whole rock geochemical data for granitic rocks (Fig. 14) in the Himalayan belt, confirming their crustal origin (Liu et al., 2020, Wu et al., 2020, Cao et al., 2022). In case of Tur4, higher Li, Be, Cr, Pb, Zn, and LREE (La, Ce) contents and variable major element compositions (Fig. 9), when compared to those of the other tourmaline types indicate that Tur4 initially also formed in the magmatic stage in a highly differentiated magma but was altered due to later interaction with a high-B external hydrothermal fluids (Harlaux et al., 2020, Ji et al., 2023, Xie et al., 2023, Cheng and Zhang, 2024). The partly high $\delta^{11}B$ values of tourmaline suggest that the fluid responsible likely derived from the metasedimentary host rocks, like marble ($\delta^{11}B = 5$ ‰,

Xie et al., 2023) or other metasedimentary materials like metapelite (Ji et al., 2023). This interpretation is supported by the observation of embayed and irregular grain boundaries of tourmaline and the occurrence of newly formed secondary minerals such as hematite (Fig. 4i) and columbite group minerals (Fig. 4m) in the spodumene pegmatite.

5.2. Records of the magma differentiation

In the Qongjiagang area, the geochronological data indicate that the granites and pegmatites formed over a short period of time from ca. 25 Ma to 22 Ma(Liu et al., 2020) indicating that granites and pegmatites are genetically related. Many authors used whole rock geochemical data of these granitic rocks to elucidate magmatic differentiation processes (Wang et al., 2017, Liu et al., 2020, Wu et al., 2020, Liu et al., 2023a). These studies show that crustal anatexis and extreme fractional crystallization are the main factors controlling the formation of the Li-rich pegmatites associated with the leucogranites. In the peraluminous, volatile-rich granite magma, the lithophile elements like Li, Cs, Ta, Nb, and Be are highly incompatible and thus remain in the melt during crystallization, leading to their strong enrichment in the residual melts which finally intrude as Lithium–Cesium–Tantalum (LCT) pegmatites.

The rare metal mineralization sequences observed in the granite and pegmatite samples from the Qongjiagang area follow a normal trend (LCT-type pegmatite), i.e. Be (beryl) mineralization prior to Li (spodumene) mineralization (Wang et al., 2017, London, 2018, Liu et al., 2020, Wu et al., 2020). Increasing Zn, Sn, Nb, and Ta contents and Zn/Sn and Nb/Ta ratios from Tur1 to Tur4 indicate a positive correlation of these elements and increasing ratios with increasing differentiation (Fig. 15a-b). In other studies, the V and Co contents in tourmaline were shown to be powerful in deciphering the relative crystallization sequence of tourmaline in granitic rocks (Yang et al., 2015b, Hu and Jiang, 2020). From Tur1 to Tur3 of our granite and pegmatite samples, both the V and Co contents increase (Fig. 15c). However, lower V and Co contents than Tur3 can't be explained by magmatic differentiation processes alone but additionally require interaction with a hydrothermal fluid, as is also suggested by variable but comparably high Li, Be, Cr, Pb, Zn, and LREE contents of Tur4 (Fig. 9). This divergent trend is also recorded by the P vs. B, Sr vs. Pb, and Sr vs. Li ratios of Tur4 (Fig. 15d-f).

Notably, the $\delta^{11}B$ values of tourmaline are commonly decreasing with increasing differentiation of the granitic magma in granite-related rare metals deposits (Zhao et al., 2021, Xie et al., 2023, Yin et al., 2023, Zhang et al., 2024, Lv et al., 2025), yet increasing during the hydrothermal alteration. The trend of decreasing $\delta^{11}B$ values with increasing differentiation is also observed for other granitic rocks of the Himalayan belt (Zhao et al., 2021, Yin et al., 2023, Zhang et al., 2024, Lv et al., 2025) including the Cuonadong deposit (Xie et al., 2023). Accordingly, the decreasing $\delta^{11}B$ values of tourmaline from Tur1 to Tur3 are attributed to successive magma differentiation (fractionation of solids and release of fluid from magma), in agreement with the geochemical and petrographic data. Increasing values $\delta^{11}B$ values from Tur3 to Tur4, also seen in the Al vs. $\delta^{11}B$ diagram (Fig. 15 g), presumably result from interaction of the Tur4 with external fluids derived from wall rocks, as also suggested by textural evidence (partly resorbed grain margins and chemical characteristics of Tur4, abundance of secondary phases in the spodumene pegmatite). T These externally derived fluids likely source from high $\delta^{11}B$ marble ($\delta^{11}B = 5$ ‰, Xie et al., 2023), which is an abundant host rock at Qongjiagang or other metasedimentary materials like metapelites (Ji et al., 2023).

Combining the new major and trace element and boron isotope data of the different type tourmalines, we can define three distinct evolutionary stages of tourmaline formation, which initially recorded magma differentiation (Tur1 to Tur3), altered by a subsequent magmatic–hydrothermal transition stage in case of Tur4 (Fig. 16): (1) Tur1 is characterized by highest $\delta^{11}B$ values, lowest Sn-Zn contents, and variable Sr-Li-Pb contents. The $\delta^{11}B$ is decreasing from core to rim, yet Li values and Sr/Y ratios display opposite trends. These data indicate that
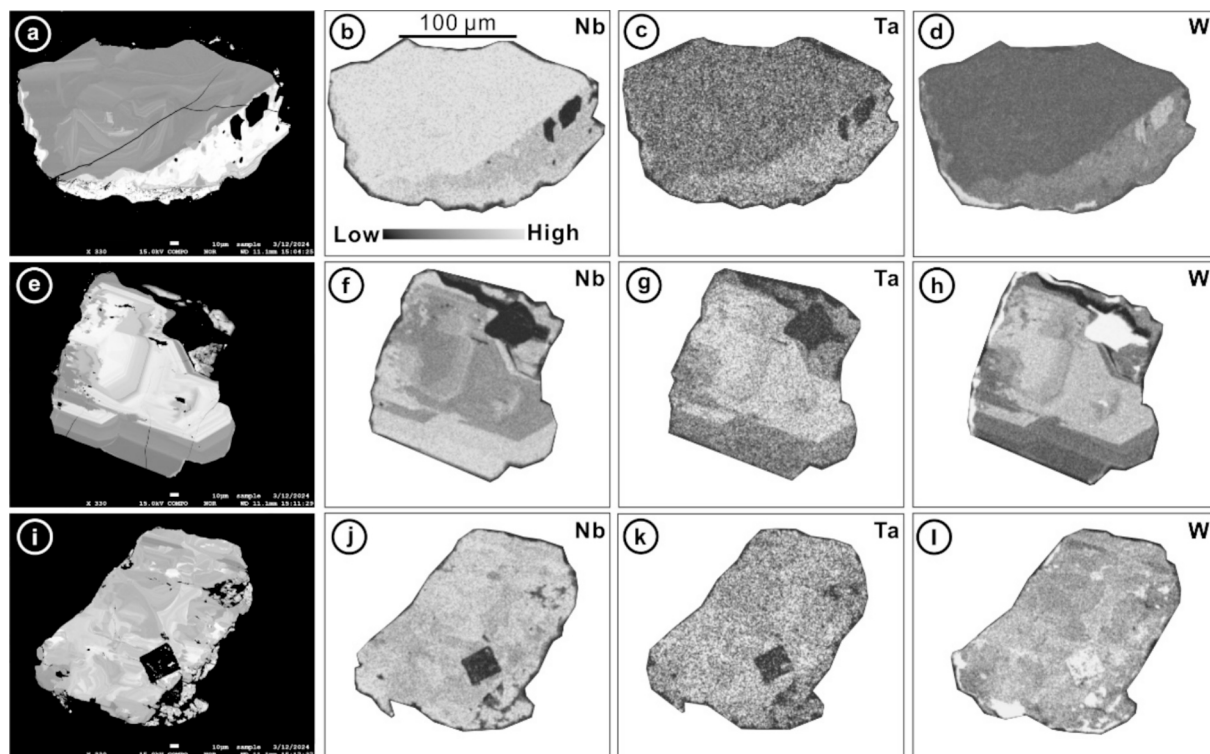
Fig. 13. The BSE graphs (dark background) and EDX mapping (white background) of CGMs from spodumene pegmatite. In the BSE graphs, light areas represent the high Ta compositions, yet dark areas represent high Nb compositions. According to their cmpositional characteristic, the CGMs were divided into three types, i.e.. type 1 with Nb-rich cores and Ta-W-rich rims (a-d), and type 2 with Ta-W-rich cores and Nb-rich rims chemical characteristics (e-h), as well as rare type 3 which exhibit no-zoning and cluttered chemical textures (i-m).
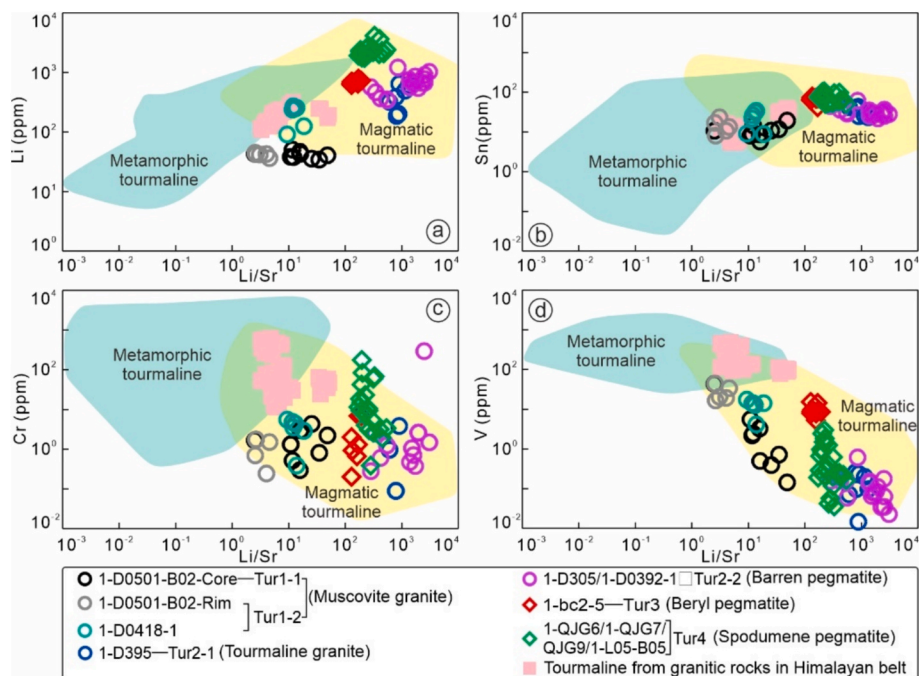

Fig. 14. Origin of tourmalines from granites and pegmatites of the Qongjiagang area. Diagrams after Harlaux et al. (2020). (a) Li vs. Li/Sr, (b) Sn vs. Li/Sr, (c) Cr vs. Li/Sr, and (d) V vs. Li/Sr.

Tur1 formed in the magmatic stage and crystallized from an early-stage low fractionation magma; Consistent with this interpretation, boron isotope compositions of Tur1 core are close to those of the metapelitic source rocks, (2) Tur2 and Tur3 display lower $\delta^{11}B$ values than Tur1, presumably resulting from successive magma differentiation and also display lower Li contents and Sn/Zn ratios, in agreement with their crystallization from a more evolved granitic magma; (3) Tur4 charac-terized by higher but strongly variable $\delta^{11}B$ values than Tur3 indicating
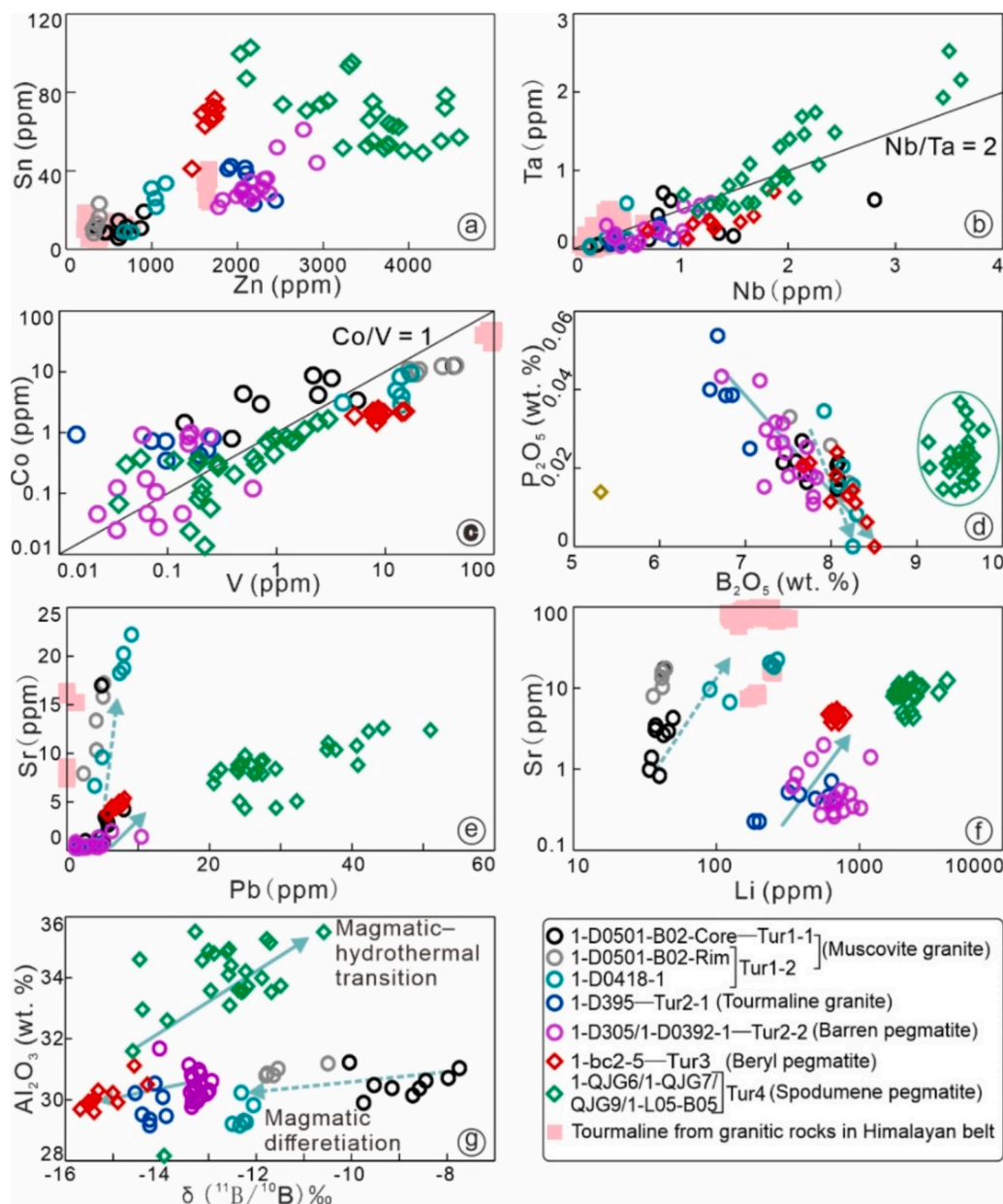
Fig. 15. Binary diagrams of selected major element oxides, trace element ratios, and $\delta^{11}B$ values of tourmalines. (a) Co vs. V, (b) Sr vs. Li, (c) Sr vs. Pb, (d) Ta vs. Nb, (e) Sn vs. Zn, (f) P_2O_5 vs. B_2O_5, (g) Al_2O_3 vs. $\delta^{11}B$. The green arrows display the proposed evolutionary trends (see text for discussion).

the influx of external fluids. The high and variable $\delta^{11}B$ values correlate with high and variable Li, Be, Nb, and Ta contents and are associated with a modal increase of minerals related to a Li-Nb-Ta mineralization (spodumene, zinnwaldite, Nb-Ta phases). Since structures (e.g., miarolitic structures and unidirectional solidification texture) related to exsolved fluids are absent in the investigated spodumene pegmatite, the composition of Tur4 is interpreted to result from its interaction with a hydrothermal fluid rather than being related to exsolution of fluid from the granitic magma at the magmatic–hydrothermal transition stage.

5.3. Rare metals enrichment and mineralization at the Qongjiagang area

Three main mechanisms are suggested to cause rare-metal enrichment in granitic-pegmatitic systems: (1) pre-enrichment of the sources (Wolf et al., 2018, Yuan et al., 2019, Romer and Kroner, 2022), (2) fractional crystallization (London, 2005, 2018), and (3) fluid release from the magma during the transition of the magmatic and

hydrothermal stage (Borisova et al., 2012, Thomas and Davidson, 2016). As discussed in chapter 5.1 and 5.2 the geochemical compositions of the four tourmaline types observed in granites and pegmatites from the Qongjiagang area reflect magmatic differentiation and magmatic–hydrothermal transition processes. According to our data, fractional crystallization processes mainly control the rare metals enrichment and mineralization at the Qongjiagang area, as was also suggested by Liu et al. (2023c), whereas hydrothermal alteration plays a minor role. These processes cause different enrichments of the rare metals, including Li, Be, Nb-Ta, and Sn, which will be discussed in the following section:

(1) **Li enrichment:** The Li contents of Tur1 are constant and comparably low (34.2–267 ppm) indicating a low Li mineralization potential of the early-stage muscovite granites (Figs. 16, 17a). Li contents increase from Tur1 to Tur2 with increasing differentiation of the magma (Figs 16 and 17a). Li contents of Tur3 are close to those of Tur2 (Figs 16 and 17a), suggesting Li saturation for Li-rich white mica in the
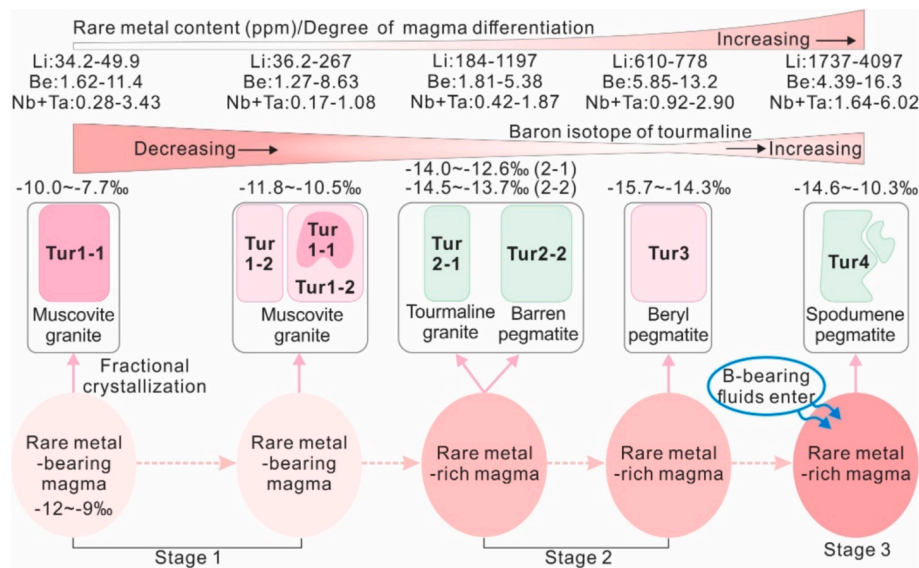
Fig. 16. Model of magma evolution, rare metal enrichment, and tourmaline formation in the granite-pegmatite system of the Qongjiagang area, Himalayan orogen.
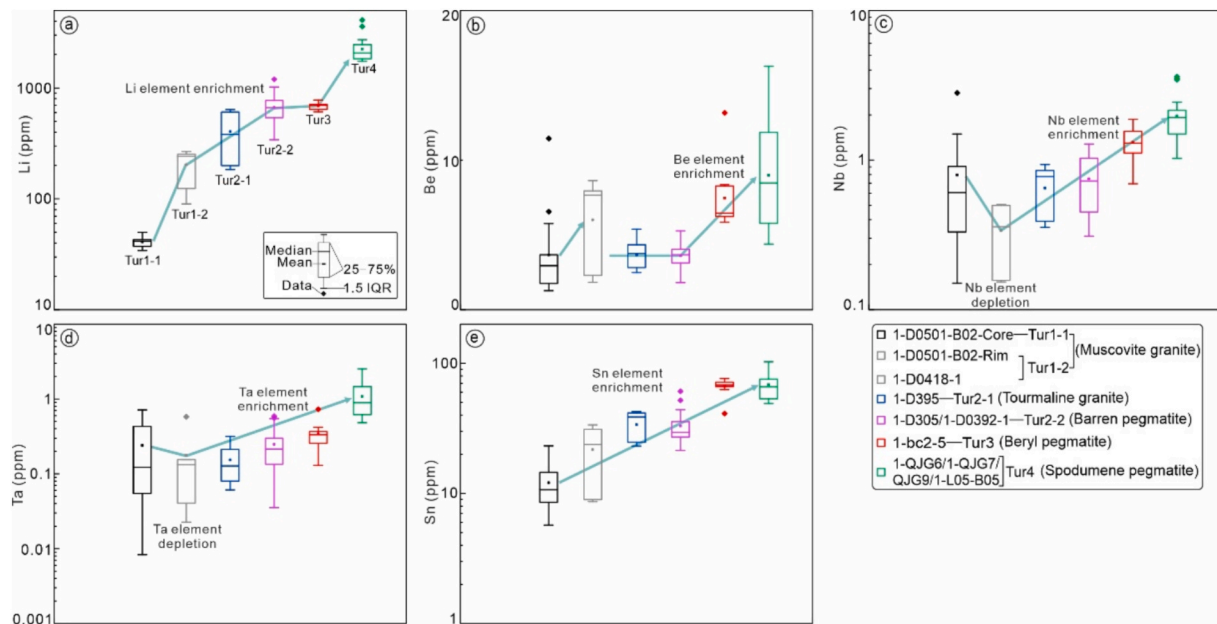

Fig. 17. Rare metal compositions of the different tourmaline types from the granites and pegmatites of the Qongjiagang area. (a-e) The Li, Be, Nb, Ta, and Sn contents.

magma. Highest but variable Li contents are recorded for Tur4 which coexists with abundant spodumene (Figs 16 and 17a). These data suggest that magma differentiation mainly controls the Li contents of tourmalines in the granites and early pegmatites. Variable Li contents of Tur4 of the spodumene pegmatites were likely caused by hydrothermal fluids, as also described for pegmatites from other occurrences (Ballouard et al., 2020, Michaud and Pichavant, 2020; Liu et al., 2023b, Xie et al., 2023).

(2) **Be enrichment:** The Be contents in a melt are generally increasing with successive differentiation (Xie et al., 2023), and reduced by fractionation of Be-bearing minerals, such as beryl (London, 2015). In the investigated samples, the Be contents increase from Tur1 to Tur4 (Figs. 16, 17b), in agreement with successive differentiation accompanied by beryl formation, as evidenced by the presence of beryl in beryl pegmatite. Notably, some high Be values are recorded for early tourmaline Tur1 (Figs. 15 and 16b). Remarkably high Be contents of 7.51 to

8.63 ppm are presumably related to an increase of Be in the magma caused by contemporaneous fractionation of Be-poor phases. A similar process is suggested to be responsible for the formation of late-stage beryl in a two-mica granite from the study by Liu et al. (2023a). Variable but high Be values of Tur4 (Figs 16 and 17b) were likely primarily controlled by magmatic differentiation, but have been altered by reaction with hydrothermal fluid.

(3) **Nb-Ta enrichment:** Columbite and tantalite are the major ores of Nb-Ta mines in the Qongjiagang area. The Nb and Ta contents of tourmaline display similar trends in the investigated granites and pegmatites (Figs 16 and 17c-d). They decrease from Tur1-1 to Tur1-2, and increase again from Tur1-2 to Tur4. The observed decreasing Nb and Ta contents from core to rim Tur1 is likely related to the early formation of Nb-Ta minerals like columbite (as Nb and Ta are more compatible in mica and columbite than in tourmaline), which is preserved as inclusions in apatite and K- feldspar in muscovite granite. Similar textures were also

observed in early stage muscovite granite from Luozha area by Shi et al. (2024), and likewise interpreted in terms of a primary Nb-Ta enrichment of the early stage magma. This subsequent trend of increasing Nb-Ta in the later stage pegmatites is consistent with successive differentiation, leading to an increasing abundance of Nb-Ta-phases in these samples. However, the chemical variability of CGMs from spodumene pegmatite suggests the enrichment process is complex of Nb-Ta.

(4) **Sn enrichment:** Previous studies have shown that the mineralized granites commonly exhibit tourmalines with high Sn contents (>19 ppm) (Hong et al., 2017). Likewise, the Sn contents of the investigated tourmalines of the granite and pegmatite samples are mostly high (5.71 to 76 ppm), suggesting a high potential for Sn resources in the Qongjiagang area. Notably, the Sn contents increase from Tur1 to Tur3, whereas the Sn contents of Tur4 are close to those of Tur3 (Figs 16 and 17f), indicating saturation of Sn (for cassiterite) in the late-stage magma that is consistent with the observation of cassiterite formation in beryl pegmatite and spodumene pegmatite.

In summary, the tourmalines from granites and pegmatites in the Qongjiagang area record independent enrichment of different rare metals in the magma with successive magma differentiation and subsequent hydrothermal alteration, with Li being strongly affected by secondary modification caused by fluid-rock interaction.

6. Conclusion

The tourmalines from different granites and pegmatites of the Qongjiagang area can be divided into four groups. Early tourmaline (Tur1) crystallized from a muscovite granite magma with a comparably low differentiation degree. Later tourmaline originates from a highly differentiated magma of tourmaline granite and barren pegmatite (Tur2), and beryl pegmatite (Tur3). The textures and chemical composition of tourmaline of spodumene pegmatite (Tur4) suggest is crystallization at the magmatic-hydrothermal transition. The B isotope ratios of tourmalines decrease from those of muscovite granite to beryl pegmatite, and increase again in tourmaline from spodumene pegmatite. Individual rare metal enrichments and changes in the boron isotopic composition of tourmaline mirror successive stages of the magma differentiation and subsequent interation with external B-rich fluids. Accordingly, changes in the chemical and isotopic composition of tourmaline could be used as indicators for the mineralization potential of the host granites and pegmatites.

Declaration of competing interest

The authors declare that they have no known competing financial interests or personal relationships that could have appeared to influence the work reported in this paper.

Acknowledgements

Appendix A. Supplementary data

Supplementary data to this article can be found online at https://doi.org/10.1016/j.oregeorev.2025.106898.

Data availability

Data will be made available on request.

References

Aikman, A.B., Harrison, T.M., Lin, D., 2008. Evidence for Early (>44 Ma) Himalayan Crustal Thickening, Tethyan Himalaya, southeastern Tibet. Earth Planet. Sci. Lett. 274, 14–23. https://doi.org/10.1016/j.epsl.2008.06.038.

Ballouard, C., Massuyeau, M., Elburg, M.A., Tappe, S., Viljoen, F., Brandenburg, J.-T., 2020. The magmatic and magmatic-hydrothermal evolution of felsic igneous rocks as seen through Nb-Ta geochemical fractionation, with implications for the origins of rare-metal mineralizations. Earth Sci. Rev. 203, 103115. https://doi.org/10.1016/j.earscirev.2020.103115.

Borisova, A.Y., Thomas, R., Salvi, S., Candaudap, F., Lanzanova, A., Chmeleff, J., 2012. Tin and associated metal and metalloid geochemistry by femtosecond LA-ICP-QMS microanalysis of pegmatite–leucogranite melt and fluid inclusions: new evidence for melt–melt–fluid immiscibility. Mineral. Mag. 76, 91–113. https://doi.org/10.1180/minmag.2012.076.1.91.

Bosi, F., 2018. Tourmaline crystal chemistry. Am. Mineral. 103, 298–306. https://doi.org/10.2138/am-2018-6289.

Cao, H.W., Pei, Q.M., Santosh, M., Li, G.M., Zhang, L.K., Zhang, X.F., et al., 2022. Himalayan leucogranites: a review of geochemical and isotopic characteristics, timing of formation, genesis, and rare metal mineralization. Earth Sci. Rev. 234, 104229. https://doi.org/10.1016/j.earscirev.2022.104229.

Capitanio, F.A., Morra, G., Goes, S., Weinberg, R.F., Moresi, L., 2010. India–Asia convergence driven by the subduction of the Greater Indian continent. Nat. Geosci. 3, 136–139. https://doi.org/10.1038/ngeo725.

Chaussidon, M., Albarède, F., 1992. Secular boron isotope variations in the continental crust: an ion microprobe study. Earth Planet. Sci. Lett. 108, 229–241. https://doi.org/10.1016/0012-821X(92)90025-Q.

Chen, X., Jiang, S.Y.R., Palmer, M., Schertl, H.-P., Cambeses, A., Hernández-Uribe, D., et al., 2023. Tourmaline chemistry, boron, and strontium isotope systematics trace multiple melt–fluid–rock interaction stages in deeply subducted continental crust. Geochim. Cosmochim. Acta 340, 120–140. https://doi.org/10.1016/j.gca.2022.11.019.

Cheng, L., Zhang, C., Zhou, Y., Horn, I., Weyer, S., Holtz, F., 2022. Experiments reveal enrichment of 11B in granitic melt resulting from tourmaline crystallisation. Geochem. Perspect. Lett. 20, 37–42. https://doi.org/10.7185/geochemlet.2206.

Cheng, L.N., Zhang, C., 2024. Boron-metasomatism and fluid evolution revealed by the chemical and boron isotopic compositions of tourmalines from the Lhozhag area, Eastern Himalaya. Lithos, 107879. https://doi.org/10.1016/j.lithos.2024.107879.

Cheng L.N., Zhang C., Yang X.S. Petrogenesis of deformed tourmaline leucogranite in the Gurla Mandhata metamorphic core complex, Southwestern Tibet. Lithos. 2020;364-365:105533.10.1016/j.lithos.2020.105533.

Ding, H.X., Li, W.T., Jiang, Y.Y., 2019. The metamorphism and the tectonic implication of the Cuonadong dome, eastern Himalaya. Acta Petrol. Sin. 3510, 312–324, 18654/1000-0569/2019.02.03 in Chinese with English abstract.

Dyar, M.D., Wiedenbeck, M., Robertson, D., Cross, L.R., Delaney, J.S., Ferguson, K., et al., 2001. Reference Minerals for the Microanalysis of Light elements. Geostand. Newslett. 25, 441–463. https://doi.org/10.1111/j.1751-908X.2001.tb00616.x.

Fan, J.J., Wang, Q., Li, J., Wei, G.J., Ma, J.L., Ma, L., et al., 2021. Boron and molybdenum isotope fractionation during crustal anatexis: Constraints from the Conadong leucogranites in the Himalayan Block, South Tibet. Geochim. Cosmochim. Acta. 297, 120–142. https://doi.org/10.1016/j.gca.2021.01.005.

Fan J.J., Wang Q., Wei G.J., Li J., Ma L., Zhang X.Z., et al. Boron and Molybdenum Isotope Evidence for Source-Controlled Compositional Diversity of Cenozoic Granites in the Eastern Tethyan Himalaya. Geochemistry, Geophysics, Geosystems. 2023;24:e2022GC010629.10.1029/2022GC010629.

Gao, L.E., Zeng, L.S., Zhao, L.H., Yan, L.L., Hou, K.J., Wang, Q., 2023. Fluid-fluxed melting in the Himalayan orogenic belt: Implications for the initiation of E-W extension in southern Tibet. GSA Bull. 136, 989–1002. https://doi.org/10.1130/b36713.1.

Gou, G.N., Wang, Q., Wyman, D.A., Xia, X.P., Wei, G.J., Guo, H.F., 2017. In situ boron isotopic analyses of tourmalines from Neogene magmatic rocks in the northern and southern margins of Tibet: evidence for melting of continental crust and sediment recycling. Solid Earth Sci. 2, 43–54. https://doi.org/10.1016/j.sesci.2017.03.003.

Han, J.S., Hollings, P., Jourdan, F., Zeng, Y.C., Chen, H.Y., 2020. Inherited Eocene magmatic tourmaline captured by the Miocene Himalayan leucogranites. Am. Mineral. 105, 1436–1440. https://doi.org/10.2138/am-2020-7608.

Harlaux, M., Kouzmanov, K., Gialli, S., Laurent, O., Rielli, A., Dini, A., et al., 2020. Tourmaline as a Tracer of Late-Magmatic to Hydrothermal Fluid Evolution: the World-Class San Rafael Tin (-copper) Deposit, Peru. Econom. Geol. 115, 1665–1697. https://doi.org/10.5382/econgeo.4762.

Hawthorne, F., Henry, D., 1999. Classification of the minerals of the tourmaline group. Eur. J. Mineral. 11, 201–215. https://doi.org/10.1127/ejm/11/2/0201.

He, S.X., Liu, X.C., Yang, L., Wang, J.M., Hu, F.Y., Wu, F.Y., 2021. Multistage magmatism recorded in a single gneiss dome: Insights from the Lhagoi Kangri leucogranites. Himalayan Orogen. Lithos. 398–399, 106222. https://doi.org/10.1016/j.lithos.2021.106222.

Henry, D.J., Dutrow, B.L., 2011. The incorporation of fluorine in tourmaline: internal crystallographic controls or external environmental influences? Can. Mineral. 49, 41–56. https://doi.org/10.3749/canmin.49.1.41.

Henry, D.J., Guidotti, C.V., 1985. Tourmaline as a petrogenetic indicator mineral: an example from the staurolite-grade metapelites of NW Maine. Am. Mineral. 70, 1–15.

Henry, D.J., Novák, M., Hawthorne, F.C., Ertl, A., Dutrow, B.L., Uher, P., et al., 2011. Nomenclature of the tourmaline-supergroup minerals. Am. Mineral. 96, 895–913. https://doi.org/10.2138/am.2011.3636.

Hodges, K.V., 2000. Tectonics of the Himalaya and southern Tibet from two perspectives. GSA Bull. 112, 324–350. https://doi.org/10.1130/0016-7606(2000)112<324:Tothas>2.0.Co;2.

Hong, W., Cooke, D., Zhang, L., Fox, N., Thompson, J., 2017. Tourmaline-rich features in the Heemskirk and Pieman Heads granites from western Tasmania, Australia: Characteristics, origins, and implications for tin mineralization. Am. Mineral. 102, 876–899. https://doi.org/10.2138/am-2017-5838.

Hou, K.J., Li, Y.H., Xiao, Y.K., Liu, F., Tian, Y.R., 2010. In situ boron isotope measurements of natural geological materials by LA-MC-ICP-MS. Chin. Sci. Bull. 55, 3305–3311. https://doi.org/10.1007/s11434-010-4064-9.

Hou, Z.Q., Zheng, Y.C., Zeng, L.S., Gao, L.E., Huang, K.X., Li, W., et al., 2012. Eocene–Oligocene granitoids in southern Tibet: Constraints on crustal anatexis and tectonic evolution of the Himalayan orogen. Earth Planet. Sci. Lett. 349–350, 38–52. https://doi.org/10.1016/j.epsl.2012.06.030.

Hu, D.L., Jiang, S.Y., 2020. In-situ elemental and boron isotopic variations of tourmaline from the Maogongdong deposit in the Dahutang W-Cu ore field of northern Jiangxi Province, South China: insights into magmatic-hydrothermal evolution. Ore Geol. Rev. 122, 103502. https://doi.org/10.1016/j.oregeorev.2020.103502.

Hu, G.Y., Gao, L.E., Zeng, L.S., Li, Y.K., 2022. Geochemical and Boron Isotopic evidence that Tourmaline Records Country Rock Assimilation of Leucogranites in the Himalayan Orogen. Acta Geol. Sin. – Engl. Ed. 96, 123–134. https://doi.org/10.1111/1755-6724.14800.

Hu, G.Y., Zeng, L.S., Gao, L.E., Liu, Q.P., Chen, H., Guo, Y.S., 2018. Diverse magma sources for the Himalayan leucogranites: evidence from B-Sr-Nd isotopes. Lithos 314–315, 88–99. https://doi.org/10.1016/j.lithos.2018.05.022.

Hu, Z.C., Zhang, W., Liu, Y.S., Gao, S., Li, M., Zong, K.Q., et al., 2015. "Wave" Signal-Smoothing and Mercury-Removing Device for Laser Ablation Quadrupole and Multiple Collector ICPMS Analysis: Application to Lead Isotope Analysis. Anal. Chem. 87, 1152–1157. https://doi.org/10.1021/ac503749k.

Huan, C., Wei, H.Z., Zhu, W.B., Palmer, M.R., Lin, H.F., Zheng, B.H., et al., 2023. Boron isotopes in tourmaline from drill core of the Jiajika granitic pegmatite type lithium deposit: Insights for granitic magma evolution and lithium enrichment. Ore Geol. Rev. 163, 105742. https://doi.org/10.1016/j.oregeorev.2023.105742.

Ji, M., Gao, X.Y., Chen, Y.X., Tu, C., Sun, G.C., Gong, B., et al., 2023. Boron isotope behavior during metamorphic dehydration and partial melting of continental crust: Constraints from tourmaline in metapelites and leucocratic dikes, Himalayan Orogen. Geochim. Cosmochim. Acta. 362, 1–21. https://doi.org/10.1016/j.gca.2023.10.018.

Kohn, M.J., 2014. Himalayan metamorphism and its tectonic implications. Annu. Rev. Earth Planet. Sci. 42, 381–419. https://doi.org/10.1146/annurev-earth-060313-055005.

Law, R.D., Searle, M.P., Godin, L., 2006. Channel flow, ductile extrusion and exhumation in continental collision zones. Geol. Soc. London.

Li G.M., Fu J.G., Guo W.K., Zhang H., Zhang L.K., Dong S.L., et al. Discovery of the Gabo granitic pegmatite-type lithium deposit in the Kulagangri Dome, eastern Himalayan metallogenic belt, and its propecting implication. Acta Petrol. Mineral.. 2022; 41: 1109-19in Chinese with English abstract.

Li, G.M., Zhang, L.K., Jiao, Y.J., Xia, X.B., Dong, S.L., Fu, J.G., et al., 2017. First discovery and implications of Cuonadong superlarge Be-W-Sn polymetallic deposit in Himalayan metallogenic belt, southern Tibet. Mineral Deposits 36, 1003.–8.10.16111/j.0258-7106.2017.04.014 in Chinese with English abstract.

Liu, C., Wang, R.C., Linnen, R.L., Wu, F.Y., Xie, L., Liu, X.C., 2023a. Continuous Be mineralization from two-mica granite to pegmatite: critical element enrichment processes in a Himalayan leucogranite pluton. Am. Mineral. 108, 31–41. https://doi.org/10.2138/am-2022-8353.

Liu, C., Wang, R.C., Wu, F.Y., Xie, L., Liu, X.C., Li, X.K., et al., 2020. Spodumene pegmatites from the Pusila pluton in the higher Himalaya, South Tibet: Lithium mineralization in a highly fractionated leucogranite batholith. Lithos 358–359, 105421. https://doi.org/10.1016/j.lithos.2020.105421.

Liu, S.Q., Zhang, G.B., Zhang, L.F., Liu, Z.Y., Xu, J., 2022. Boron isotopes of tourmalines from the central Himalaya: Implications for fluid activity and anatexis in the Himalayan orogen. Chem. Geol. 596, 120800. https://doi.org/10.1016/j.chemgeo.2022.120800.

Liu, T., Jiang, S.Y., Su, H.M., Zhao, K.D., Zhao, H.D., Cao, M.Y., 2023b. Tourmaline as a tracer of magmatic-hydrothermal evolution and potential Nb-Ta-(WSn) mineralization from the Lingshan granite batholith, Jiangxi province, southeast China. Lithos 438–439, 107016. https://doi.org/10.1016/j.lithos.2022.107016.

Liu, Y.C., Qin, K.Z., Zhao, J.X., Zhou, Q.F., Shi, R.Z., He, C.T., et al., 2023c. Feldspar traces mineralization processes in the Qongjiagang giant lithium ore district, Himalaya, Tibet. Ore Geol. Rev. 157, 105451. https://doi.org/10.1016/j.oregeorev.2023.105451.

Liu, Y.S., Hu, Z.C., Gao, S., Günther, D., Xu, J., Gao, C.G., et al., 2008. In situ analysis of major and trace elements of anhydrous minerals by LA-ICP-MS without applying an internal standard. Chem. Geol. 257, 34–43. https://doi.org/10.1016/j.chemgeo.2008.08.004.

Liu Z.C., Wu F.Y., Liu X.C., Wang J.G. The mechanisms of fractional crystallization for the Himalayan leucogranites. Acta Petrologica Sinica. 2020b;36:3551-71.18654/1000-0569/2020.12.01 in Chinese with English abstract.

London, D., 2005. Granitic pegmatites: an assessment of current concepts and directions for the future. Lithos 80, 281–303. https://doi.org/10.1016/j.lithos.2004.02.009.

London, D., 2015. Reading Pegmatites: Part 1—What Beryl says. Rocks Miner. 90, 138–153. https://doi.org/10.1080/00357529.2014.949173.

London, D., 2018. Ore-forming processes within granitic pegmatites. Ore Geol. Rev. 101, 349–383. https://doi.org/10.1016/j.oregeorev.2018.04.020.

Lv, J.T., Chen, X., Jiang, J.S., Schertl, H.P., Cao, L., Jiang, X.J., 2025. Chemical and boron isotope composition of multiple generations of tourmaline from the

Nassarawa lithium-rich pegmatites, Nigeria: Implications for the mechanism of lithium enrichment. Lithos 494–495, 107936. https://doi.org/10.1016/j.lithos.2024.107936.

Ma, L., Wang, Q., Kerr, A.C., Li, Z.X., Dan, W., Yang, Y.N., et al., 2022. Eocene magmatism in the Himalaya: Response to lithospheric flexure during early Indian collision? Geology 51, 96–100. https://doi.org/10.1130/g50438.1.

Michaud, J.a.-S., Pichavant, M., 2020. Magmatic fractionation and the magmatic-hydrothermal transition in rare metal granites: evidence from Argemela (Central Portugal). Geochim. Cosmochim. Acta 289, 130–157. https://doi.org/10.1016/j.gca.2020.08.022.

Qin, K.Z., Zhao, J.X., He, C.T., Shi, R.Z., 2021. Discovery of the Qongjiagang giant lithium pegmatite deposit in Himalaya, Tibet, China. Acta Petrol. Sin. 37, 3277–3286, 10.18654/1000-0569/2021.11.02 in Chinese with English abstract.

Romer R.L., Kroner U. Provenance control on the distribution of endogenic Sn-W, Au, and U mineralization within the Gondwana-Laurussia plate boundary zone. In: KUIPER Y.D., MURPHY J.B., NANCE R.D., STRACHAN R.A., THOMPSON M.D., editors. New Developments in the Appalachian-Caledonian-Variscan Orogen: Geological Society of America; 2022. p. 0.

Searle, M.P., Treloar, P.J., 2019. Introduction to Himalayan tectonics: a modern synthesis. Geol. Soc. Lond. Spec. Publ. 483, 1–17. https://doi.org/10.1144/SP483-2019-20.

Shi, R.Z., Zhao, J.X., He, C.T., Qin, K.Z., Zhao, Y.N., Cao, M.J., et al., 2024. The formation of mineral inclusions in accessory minerals from Qongjiagang pegmatite-type Li deposit and the implications to melt-fluid characteristics. Acta Petrol. Sin. 40, 450–464. https://doi.org/10.18654/1000-0569/2024.02.05.

Singh S. Himalayan Magmatism through space and time. International Union of Geological Sciences. 2020;43:358-68.10.18814/epiiugs/2020/020022 eng.

Thomas, R., Davidson, P., 2016. Revisiting complete miscibility between silicate melts and hydrous fluids, and the extreme enrichment of some elements in the supercritical state — Consequences for the formation of pegmatites and ore deposits. Ore Geol. Rev. 72, 1088–1101. https://doi.org/10.1016/j.oregeorev.2015.10.004.

Van Hinsberg, V.J., 2011. Preliminary experimental data on trace-element partitioning between tourmaline and silicate melt. Can. Mineral. 49, 153–163. https://doi.org/10.3749/canmin.49.1.153.

Van Hinsberg, V.J., Henry, D.J., Dutrow, B.L., 2011a. Tourmaline as a Petrologic Forensic Mineral: a Unique Recorder of its Geologic past. Elements 7, 327–332. https://doi.org/10.2113/gselements.7.5.327.

Van Hinsberg, V.J., Henry, D.J., Marschall, H.R., 2011b. Tourmaline: an ideal indicator of its host environment. Can. Mineral. 49, 1–16. https://doi.org/10.3749/canmin.49.1.1.

Wang, J.M., Wu, F.Y., Zhang, J.J., Khanal, G., Yang, L., 2022. The Himalayan Collisional Orogeny: a Metamorphic Perspective. Acta Geologica Sinica - English Edition. 96, 1842–1866. https://doi.org/10.1111/1755-6724.15022.

Wang, R.C., Wu, F.Y., Xie, L., Liu, X.C., Wang, J.M., Yang, L., et al., 2017. A preliminary study of rare-metal mineralization in the Himalayan leucogranite belts, South Tibet. Sci. China Earth Sci. 60, 1655–1663. https://doi.org/10.1007/s11430-017-9075-8.

Weller, O.M., Mottram, C.M., St-Onge, M.R., Möller, C., Strachan, R., Rivers, T., et al., 2021. The metamorphic and magmatic record of collisional orogens. Nat. Rev. Earth Environ. 2, 781–799. https://doi.org/10.1038/s43017-021-00218-z.

Wolf, M., Romer, R.L., Franz, L., López-Moro, F.J., 2018. Tin in granitic melts: the role of melting temperature and protolith composition. Lithos 310–311, 20–30. https://doi.org/10.1016/j.lithos.2018.04.004.

Wu, F.Y., Ji, W.Q., Wang, J.G., Liu, C.Z., Chung, S.L., Clift, P.D., 2014. Zircon U-Pb and Hf isotopic constraints on the onset time of India-Asia collision. Am. J. Sci. 314, 548–579. https://doi.org/10.2475/02.2014.04.

Wu, F.Y., Liu, X.C., Liu, Z.C., Wang, R.C., Xie, L., Wang, J.M., et al., 2020. Highly fractionated Himalayan leucogranites and associated rare-metal mineralization. Lithos 352–353, 105319. https://doi.org/10.1016/j.lithos.2019.105319.

Xie G.Z., Yan H.B., Zhang R.Q., Wang K., Zhang L.P. Hydrothermal fluid evolution in the Cuonadong Sn–W–Be polymetallic deposit, southern Tibet: indicated bye in–situ element and boron isotope compositions of tourmaline. Frontiers in Earth Sci. 2023; 11.10.3389/feart.2023.1106871.

Xiong, J.W., Chen, Y.X., Ma, H.Z., Schertl, H.P., Zheng, Y.F., Zhao, K.D., 2022. Tourmaline boron isotopes trace metasomatism by serpentinite-derived fluid in continental subduction zone. Geochim. Cosmochim. Acta 320, 122–142. https://doi.org/10.1016/j.gca.2022.01.003.

Yang, S.Y., Jiang, S.Y., Palmer, M.R., 2015a. Chemical and boron isotopic compositions of tourmaline from the Nyalam leucogranites, South Tibetan Himalaya: Implication for their formation from B-rich melt to hydrothermal fluids. Chem. Geol. 419, 102–113. https://doi.org/10.1016/j.chemgeo.2015.10.026.

Yang, S.Y., Jiang, S.Y., Zhao, K.D., Dai, B.Z., Yang, T., 2015b. Tourmaline as a recorder of magmatic–hydrothermal evolution: an in situ major and trace element analysis of tourmaline from the Qitianling batholith, South China. Contrib. Miner. Petrol. 170, 42. https://doi.org/10.1007/s00410-015-1195-7.

Yin, A., Dubey, C.S., Kelty, T.K., Gehrels, G.E., Chou, C.Y., Grove, M., et al., 2006. Structural evolution of the Arunachal Himalaya and implications for asymmetric development of the Himalayan orogen. Curr. Sci. 90, 195–206.

Yin R., Huang X.L., Wang R.C., Wei G.J., Xu Y.G., Wang Y., et al. Magmatic–hydrothermal evolution of the Koktokay No. 3 pegmatite, Altai, northwestern China: Constraints from in situ boron isotope and chemical compositions of tourmaline. Lithos. 2023; 462-463: 107398. Doi: 10.1016/j.lithos.2023.107398.

Yu, D.S., Yan, H.B., Wang, S.J., Xu, D.R., Wang, Z.L., Ma, C., et al., 2024. Chemical and boron isotopic compositions of tourmaline from the pegmatite in Ke'eryin rare metal orefield, Eastern Tibet: Implications for pegmatitic evolution. J. Geochem. Explor. 262, 107475. https://doi.org/10.1016/j.gexplo.2024.107475.

Yuan, S.D., Williams-Jones, A.E., Romer, R.L., Zhao, P.L., Mao, J.W., 2019. Protolith-Related thermal Controls on the Decoupling of Sn and W in Sn-W Metallogenic Provinces: Insights from the Nanling Region, China. Econom. Geol. 114, 1005–1012. https://doi.org/10.5382/econgeo.4669.

Zhang, X.Y., Wang, H., Bai, H.Y., Wang, K.Y., Huang, L., 2024. Tourmaline geochemical and boron isotopic compositions of the Bailongshan rare-metal pegmatite deposit: Implications for magmatic-hydrothermal evolution of the West Kunlun Orogen (NW China). Ore Geol. Rev. 166, 105894. https://doi.org/10.1016/j.oregeorev.2024.105894.

Zhao, H.D., Zhao, K.D., Palmer, M.R., Jiang, S.Y., 2019. In-situ elemental and boron isotopic variations of tourmaline from the Sanfang granite, South China: Insights into magmatic-hydrothermal evolution. Chem. Geol. 504, 190–204. https://doi.org/10.1016/j.chemgeo.2018.11.013.

Zhao, H.D., Zhao, K.D., Palmer, M.R., Jiang, S.Y., Chen, W., 2021. Magmatic-Hydrothermal Mineralization Processes at the Yidong Tin Deposit, South China: Insights from In Situ Chemical and Boron Isotope changes of Tourmaline. Econ. Geol. 116, 1625–1647. https://doi.org/10.5382/econgeo.4868.

Zheng, Y.Y., Chen, X., Gao, S.B., Li, H.Q., Jiang, X.J., Zheng, S.L., 2024a. Discovery and Prospecting significance of Zhaguopu Li-Nb-Ta Deposit in the Western Himalayan Metallogenic Belt. Earth Sci. 49, 1555–1564, 10.3799/dqkx.2024.035 in Chinese with English abstract.

Zheng, Y.Y., Chen, X., Palmer, M.R., Zhao, K.D., Hernández-Uribe, D., Gao, S.B., et al., 2024b. Magma mixing and magmatic-to-hydrothermal fluid evolution revealed by chemical and boron isotopic signatures in tourmaline from the Zhunuo–Beimulang porphyry Cu-Mo deposits. Miner. Deposita. https://doi.org/10.1007/s00126-024-01255-6.

Zhou, Q., Li, W.C., Wang, G.C., Liu, Z., Lai, Y., Huang, J.H., et al., 2019. Chemical and boron isotopic composition of tourmaline from the Conadong leucogranite-pegmatite system in South Tibet. Lithos 326–327, 529–539. https://doi.org/10.1016/j.lithos.2019.01.003.

Zong, K.Q., Klemd, R., Yuan, Y., He, Z.Y., Guo, J.L., Shi, X.L., et al., 2017. The assembly of Rodinia: the correlation of early Neoproterozoic (ca. 900Ma) high-grade metamorphism and continental arc formation in the southern Beishan Orogen, southern Central Asian Orogenic Belt (CAOB). Precambr. Res. 290, 32–48. https://doi.org/10.1016/j.precamres.2016.12.010.